Journal of Molecular Structure 1351 (2026) 144223

Contents lists available at ScienceDirect

Journal of Molecular Structure

journal homepage: www.elsevier.com/locate/molstr

Synthesis, structural analysis, and computational investigations of metronidazole and climbazole derivatives

Ebrar Nur Özkan [a,*], Melek Gökmen Karakaya [b,*], Özlem Gündoğdu Aytaç [a,c,*], Ertan Şahin [a], Abdullah Menzek [a,d]

[a] Department of Chemistry, Faculty of Sciences, Ataturk University, Erzurum 25240, Türkiye
[b] Laboratory Technology Program, Department of Chemistry and Chemical Processing Technologies, Banaz Vocational School, Uşak University, Uşak 64500, Türkiye
[c] Department of Food Technology, Kaman Vocational School, Kırşehir Ahi Evran University, Kırşehir 40300, Türkiye
[d] Department of EADM, Faculty of Health Sciences, Ardahan University, Ardahan 75002, Turkiye

ARTICLE INFO

Keywords:
Climbazole
Metroindazol
Single crystal XRD
Hirshfeld surface analysis
Molecular docking

ABSTRACT

This study details the synthesis, characterization, and in silico studies of two new molecules, 4-(3-(2-methyl-5-nitro-1*H*-imidazol-1-yl)propyl)phthalonitrile (**5**) and 1-(4-chloro-2-nitrophenoxy)-1-(1*H*-imidazol-1-yl)-3,3-dimethylbutan-2-one (**7**), which are derivatives of metronidazole and climbazole. The structural description of nitro-climbazole (**7**) was confirmed by single crystal X-ray analysis, which revealed the monoclinic crystal system with the space group $P2_1/n$. Complementary to the experimental findings, computational studies were carried out using Density Functional Theory (DFT) with Gaussian 09 software. These calculations, including geometry optimization and frequency analysis, were performed at the mPW1PW91/6-311G(d,p) level for molecule **5** and at the wb97xd/6-311G(d,p) level for molecule **7**. These analyses yielded important data regarding the stability and electronic structures of the molecules. Hirshfeld surface analysis based on CIF data obtained from the crystal structure **7** revealed intermolecular H•••H, O•••H, and Cl•••H contacts, demonstrating the contribution of these interactions to the stability of the crystal structure. Energy framework analyses elucidated the internal interactions of the structure by visualizing the cohesive forces within the crystal lattice. Frontier Molecular Orbital (FMO) analysis of molecules **5** and **7** revealed the distribution of their HOMO and LUMO orbitals, providing insights into their electronic behavior and reactivity potential. Furthermore, surface Electrostatic Potential (ESP) mapping identified electron-rich and electron-poor regions within the molecules, providing complementary information regarding potential biological interaction sites. Furthermore, their antibacterial and antifungal activities were investigated using in silico methods. This study, which combines experimental and theoretical approaches, comprehensively reveals the structural and electronic properties of the synthesized molecules.

1. Introduction

Bacterial pathogen infections, which have become quite common in recent years, pose a danger to public health [1]. Nitrogen-containing heterocyclic analogs have garnered significant attention in drug discovery owing to their well-established pharmacological and therapeutic activities across various medical applications [2]. Among heterocyclic frameworks, triazole derivatives, particularly those containing nitro substituents, have gained significant attention in synthetic and medicinal chemistry due to their versatile reactivity and broad biological potential. Nitro-substituted triazoles serve as valuable scaffolds in the design of novel drug candidates, as the nitro group modulates the electronic density of the triazole ring, thereby improving binding affinity and selectivity toward specific biological targets [3]. These compounds exhibit a wide spectrum of pharmacological activities, including antimicrobial, antifungal, anticancer, anti-inflammatory, and antiviral properties [3,4]. In recent years, Density Functional Theory (DFT) calculations have been extensively applied to investigate the structural, electronic, and spectroscopic properties of nitro-triazole derivatives, providing deeper insights into their chemical reactivity, molecular stability, and frontier molecular orbitals [5]. Furthermore, in silico molecular docking and molecular dynamics studies play a crucial role in predicting the binding interactions of these compounds with target biomolecules, thereby accelerating drug discovery and reducing

* Corresponding authors.
E-mail addresses: ebrarnur.ozkan89@gmail.com (E.N. Özkan), melek.karakaya@usak.edu.tr (M.G. Karakaya), ogundogdu@ahievran.edu.tr (Ö.G. Aytaç).

https://doi.org/10.1016/j.molstruc.2025.144223
Received 26 July 2025; Received in revised form 20 September 2025; Accepted 30 September 2025
Available online 30 September 2025

experimental costs [6]. The integration of synthetic, computational, and biological approaches thus offers a comprehensive strategy for understanding structure–activity relationships (SARs) and developing potent triazole-based therapeutic agents [7]. In recent years, multifunctional heterocyclic compounds and hybrid nanomaterials have also emerged as promising candidates for improving antibacterial and antifungal treatments, owing to their tunable structures and enhanced bioactivity [4]. Many heterocyclic molecules bearing a five-membered ring are known to be rich in biological activity [8,9]. Miconazole (**1**) and ketoconazole (**2**) including imidazole ring unit are used as antifungal drugs (Fig. 1).

Metronidazole (**3**) (**MTZ**) has long been used in the treatment of various infectious diseases, such as protozoal, microbial, and bacterial infections [10–13]. It has also found application in cancer chemotherapy and radiotherapy. In radiotherapy, in particular, metronidazole is more effective against hypoxic (oxygen-deficient) tumor cells due to its high electron affinity and is therefore used as a hypoxic cell radiosensitizer. The biological activity of metronidazole is directly related to its electron affinity and interaction with DNA [14,15].

Climbazole (**6**) (**CBZ**), including an imidazole unit, inhibits the growth of fungi and some microorganisms [16]. It is used both as an anti-hair loss treatment and as an anti-dandruff agent in shampoos [17]. We determined that racemic alcohols formed by reduction of the carbonyl group in **6** can be used in the removal of Fe^{+2} from wastewater [18]. Metroindazole, an imidazole derivative, is used usually as drug for variety of infections caused by anaerobic bacteria and certain parasites. A nitro group is found at the imidazole ring of Metroindazole, It is known that drugs containing nitro groups provide effective treatments against some diseases [19]. Therefore, biological evaluations of novel molecules containing nitro groups are important [19,20].

Hirshfeld surface analysis is a method used to visualize and study intermolecular interactions in crystal structures. This analysis is particularly effective in characterizing weak interactions such as hydrogen bonds and C—H contacts. The nature and contribution of intermolecular contacts can be quantitatively summarized through two-dimensional fingerprint plots. Hirshfeld surfaces and the fingerprint plots obtained from these surfaces provide detailed analysis of interactions between neighboring atoms and also play an important role in assessing molecular packing and the accuracy of the crystal structure [21–23].

In this study, new molecules **5** and **7** were synthesized from each of the pharmaceutical molecules **3** and **6**. These molecules were purified, then structurally characterized, and their potential antibacterial and antifungal activities were evaluated using in silico methods.

2. Experimental section details

2.1. Chemistry

2.1.1. General information

All chemicals and organic solvents were purchased from commercial sources (Merck, Sigma-Aldrich) and used without any purifications thin. Bruker 400 MHz NMR spectrometer (^{1}HNMR 400 MHz, ^{13}CNMR 100 MHz) was used for NMR analyses. Melting points of the products were determined with a GallenKamp MPD 350 capillary melting point device. FTIR spectra were performed on a Perkin Elmer Spectrum Two spectrophotometer equipped with ATR apparatus. Single-crystal X-ray diffraction data were collected on a Rigaku R-AXIS RAPID-S diffractometer equipped with a four-circle, two-dimensional area imaging plate detector. HRMS: electron spray technique (*M*+/M-) from the soln. in MeOH (Waters LCT Premier TM XE UPLC/MS TOF) (Manchester, UK) [24,25].

2.1.2. Synthesis

*2.1.2.1. Synthesis of 4-(2-(2-methyl-5-nitro-1H-imidazol-1-yl)ethoxy) phthalonitrile (**5**).* A solution of metronidazole (**3**) (400 mg, 2.34 mmol) and 4-nitrophthalonitrile (**4**) (404 mg, 2.34 mmol) in dimethyl formamide (DMF) (20 mL) in a round-bottomed flask (100 mL) was prepared at ambient temperature under nitrogen. After the stirred solution was refluxed under nitrogen for 10 min, finely powdered ground anhydrous K_2CO_3 (1.62 g, 11.7 mmol) was added to the reaction content piece by piece within 1.5 h. The reaction mixture was refluxed for an additional 5 days and then poured into a water-ice mixture. Formed mixture was stirred for 1 day and then extracted with ethyl acetate (2 × 50 mL). Combined organic phases dried over Na_2SO_4, filtered, and the solvent was removed in the evaporator. Reaction product **5** (65 %, 503.60 mg, 1.52 mmol) was obtained. M.p. 61.3–65.2 °C; R_f = 0.75 (EtOAc/hexane = 3/7); ^{1}H-NMR (400 MHz, $(CD_3)_2CO$): 7.98 (d, A part of AB system, J = 8.8 Hz, aromatic, 1H), 7.93 (s, aromatic, 1H), 7.69 (d, J = 2.3 Hz, aromatic, 1H), 7.93 (dd, B part of AB system, J = 8.8, 2.3 Hz, aromatic, 1H), 4.93 (t, J = 4.8 Hz, CH_2, 2H), 4.69 (t, J = 4.8 Hz, CH_2, 2H), 2.64 (s, CH_3, 3H); ^{13}CNMR [100 MHz, $(CD_3)_2CO$)]: 162.37, 152.75, 136.51, 133.49, 120.88, 120.83, 177.76, 116.57, 116.13, 108.15, 68.75, 46.33, 14.47; FTIR (ATR) 3103, 3052, 3010, 2929, 2800, 2685, 2582, 2545, 2521, 2234, 2223, 1919, 1645, 1603, 1566, 1485, 1433, 1382, 1323, 1250, 1173, 1098, 862, 832, 667, 525 cm^{-1}; HRMS (APCI – TOF) (*m/z*) calcd for $[(C_{14}H_{11}N_5O_3) + H]^+$: 298.09401; found: 298.09337.

*2.1.2.2. Synthesis of 1-(4-chloro-2-nitrophenoxy)-1-(1H-imidazol-1-yl)-3,3-dimethylbutan-2-one (**7**).* Concentred nitric acid (65 %, 3 mL) and sulphuric acid (98 %, 2.5 mL) were added to two-necked round bottom flask (500 mL), and stirred mixture was cooled for 30 min by ice-water bath. Then a cold solution of climbazole (**6**) (1.0 g, 3.416 mmol) in CH_2Cl_2 (300 mL) were added to the reaction medium, and a double phase was appeared in the flask. After the mixture was stirred for two weeks at ambient temperature and was poured into separate funnel, organic phase was seperated and a cold aqueous solution of $NaHCO_3$ was slowly added to organic phase for neutralization of reaction mixture. Organic phase separated again is washed with brine (3 × 30 mL), dried

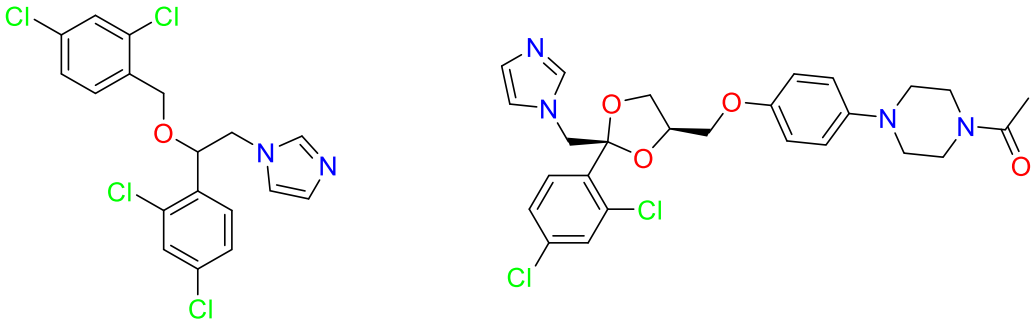

1 Miconazole **2** Ketoconazole

Fig. 1. Chemical structures of miconazole and ketoconazole.

over anhydrous Na_2SO_4 and the solvent was removed under vacuum. The residue was submitted to silica gel (10 g) column chromatography with EtOAc/hexane (30/70) elution. After the product having a light yellow solid and including trace amount of **6**, was crystallized from CH_2Cl_2, ethyl ether and petroleum ether, molecule **7** (320 mg, 28 %) was obtained as pure. M.p. 113–115 °C; $R_f = 0.40$ (EtOAc/hexane = 3/7); ^{1}HNMR (400 MHz, $CDCl_3$): 7.87 (d, $J = 2.6$ Hz 1H), 7.56 (bs,1H), 7.35 (dd, $J = 8.8$, 2.6 Hz 1H), 7.12–7–00 (m, 2H), 6.64 (bs,1H), 6.44 (d, $J = 8.8$ Hz, 1H), 1.20 (bs, 9H); ^{13}CNMR (100 MHz, $CDCl_3$): 203.08 (CO), 146.78, 143.33 (C), 137.47 (CH), 134.66 (CH and C), 131.43 (CH), 126.07 (CH), 124.93, 118.44 (CH), 82.51 (OCH), 44.42 (C), 26.27 (3 CH_3);); FTIR (ATR) 3151, 3118, 3105, 3084, 2970, 2937, 2907, 2872, 1731 (*C = O*), 1607 (*C = C* aromatic), 1569, 1531, 1514, 1477, 1398, 1373, 1338, 1284, 1244, 1213, 1150, 1104, 1068, 1036, 1019, 971, 922, 882, 839, 825, 785, 753, 683, 660, 650, 629, 594, 561, 487 cm^{-1}; HRMS (APCI – TOF) (*m/z*) calcd for $[(C_{15}H_{16}ClN_3O_4) + H]^+$: 337.08293. found: 337.08276.

2.2. Crystal structure determination

The climbazole derivative **7** crystal were grown from ethanol at ambient temperature by the slow evaporation technique. For structure determination, a single crystal of molecule **7** was analyzed on a Rigaku R-AXIS RAPID-S diffractometer equipped with a four-circle, two-dimensional area imaging plate detector. Data acquisition was carried out using graphite-monochromated Mo-Kα radiation (λ = 0.71073 Å) and an oscillatory scanning technique with Δω = 5° for each image. Lattice parameters were determined by the least-squares method based on reflections satisfying the criterion $F^2 > 2\sigma(F^2)$. Integration of reflection intensities, Lorentz and polarization corrections, and cell refinement were performed using CrystalClear software (Rigaku/MSC Inc., 2005) [26]. In solving the crystal structure, direct methods were used to determine the positions of the heaviest atoms, using the SHELXS-2013 program [27]. The remaining non-hydrogen atoms were refined using full-matrix least-squares refinement cycles on the F^2 values using the SHELXL-2013 program [27]. All non-hydrogen atoms were refined using anisotropic displacement parameters. Common isotropic displacement factors were assigned to the hydrogen atoms, and these atoms were placed in idealized geometric positions and included in the final refinement process. No chemically significant residual electron density was observed in the final difference Fourier maps. Crystal and structure refinement data of the molecules **7** was given in Table 1.

Table 1
Crystal and structure refinement data of the molecules **7**.

Empirical formula	$C_{15}H_{16}N_3O_4$ Cl
Formula weight	337.76
Temperature (K)	293(2)
Wavelength (Å)	0.71073
Crystal system	monoclinic
Space group	$P2_1/n$
Unit cell dimensions	$a = 12.4015(3)$ Å $\alpha = 90°$ $b = 8.0746(2)$ Å $\beta = 95.990(2)°$ $c = 16.3510(4)$ Å $\gamma = 90$
Volume ($Å^3$)	1628.40(7)
Z	4
Density (calculated) (g/cm^3)	1.378
Absorption coefficient (mm^{-1})	2.293
F(000)	704
Theta range for data collection	4.3 to 72.3°
Index ranges	$-15 \le h \le 15$, $-9 \le k \le 9$, $-20 \le l \le 20$
Reflections collected	23,879
Independent reflections	3203 [*R*(int) = 0.045]
Data Completeness (%)	99.7
Refinement method	Full-matrix least-squares on F^2
Data/restraints/parameters	2681/0/212
Goodness-of-fit on F^2	1.091
Final R indices [I > 2sigma(I)]	*R*1 = 0.051, w*R*2 = 0.129
R indices (all data)	*R*1 = 0.061, w*R*2 = 0.137
Largest diff. peak and hole	0.431 and 0.345

CCDC-2472171 (**7**) number contains the supplementary crystallographic data. These data are provided free of charge via the joint CCDC/FIZ Karlsruhe deposition service www.ccdc.cam.ac.uk/structures.

2.3. Computational studies

2.3.1. Density functional theory (DFTs) computations

DFT-based calculations are becoming increasingly important in theoretical medicinal chemistry. Density Functional Theory (DFT) assumes that a system can determine its ground-state energy and other atomic properties based solely on its electronic density [28]. DFT has proven its effectiveness in the structural analysis of medicinal molecules, particularly with its success in accurately predicting the molecular geometries of small organic molecules. The high degree of agreement between theoretical data obtained with DFT and experimental findings has been demonstrated in numerous studies supporting the reliability and applicability of this method. Therefore, DFT stands out as a powerful theoretical tool for investigating electron affinity, ionization energy, relative energy, and metal-ligand bond strengths [29].

In our study, DFT calculations were performed using specific levels of theory tailored for each molecule. For molecule **5,** the mPW1PW91/6–311G(d,p) level of theory was employed. The mPW1PW91 functional is a modified Perdew-Wang exchange functional combined with the Perdew-Wang correlation functional, known for its robust performance in predicting thermochemical properties and geometries across a wide range of molecular systems. The 6–311G(d,p) basis set, being a triple-zeta basis set with polarization functions on both heavy atoms (d) and hydrogens (p), provides a more flexible description of the electron density, leading to more accurate results, especially for systems involving hydrogen bonding or intricate electronic structures.

For molecule **7,** the wb97xd/6–311G(d,p) basis set was utilized. The wb97xd functional is a range-separated hybrid functional that includes empirical dispersion corrections (indicated by 'xd'). This choice is particularly advantageous for systems where non-covalent interactions, such as van der Waals forces, play a significant role, as it accurately accounts for long-range electron correlation effects which are crucial for molecular stacking and binding. The 6–311G(d,p) basis set was again chosen for its enhanced accuracy and flexibility in describing the molecular orbitals. The use of different functionals for molecule **5** and molecule **7** stems from the need to optimize computational accuracy for the specific chemical properties or interactions dominant in each molecule, ensuring the most reliable results for their distinct characteristics. This selection is particularly important for molecule **7**′s crystalline and halogenated nature, allowing for a more accurate modeling of intermolecular interactions.

In addition to physical parameters, global reactivity descriptors of the synthesized molecules **5** and **7** were assessed. Gaussian 09 [30] software was used to carry out DFT calculations on multi-core systems, and GaussView 6 [https://gaussian.com/wp-content/uploads/dl/gv6.pdf] was used to visualize optimized structures.

2.3.2. Molecular docking

Molecular docking studies are essential in drug design and pharmacology, as they offer detailed insights into protein–ligand interactions and efficiently identify potential binding sites. This approach is widely recognized as a reliable and fast technique for evaluating molecular interactions, making it particularly valuable in the early stages of drug discovery and development [31]. In our study, in silico molecular docking interactions of molecules **5** and **7** selected proteins were analyzed using AutoDock Tools.

The molecular structures of the target molecules were designed and

optimized using ChemDraw 19.0. These structures were then converted into three-dimensional (3D) molecular models and saved in PDB (Protein Data Bank) format using Avogadro, thus enabling proper geometry optimization and energy minimization. According to the experimental procedure and literature, target proteins were selected as human lanosterol 14alpha-demethylase (CYP51) (PDB: 3LD6) [32], the thioredoxin reductase from *Entamoeba histolytica* with NADP (PDB ID: 4CCQ) [33] and *Candida glabrata* dihydrofolate reductase complexed with NADPH and 6-methyl-5-[3-methyl-3-(3,4,5-trimethoxyphenyl)but-1-yn-1-yl] pyrimidine-2,4-diamine (UCP115A) (PDB: 3QLY) [34,35] and 3D-pdb versions of the receptors were retrieved from the protein database (https://www.rcsb.org/).

Before molecular docking, ligand and protein structures were prepared using AutoDock Tools 1.5.7. This preparation process included the removal of water molecules, the addition of polar hydrogen atoms, and the assignment of appropriate docking parameters. Both ligands and proteins were then converted to the PDBQT file format required for docking simulations in AutoDock. Molecular docking analyses were performed to predict binding affinity and interaction modes between the ligands and the active sites of the target proteins. The grid parameters were selected as 60 × 60 × 60, Å x, y, z dimensions, 0.553 Å space. 42.287, 4.969, 1.219 x, y, z centers for human lanosterol 14alpha-demethylase (CYP51) (PDB: 3LD6), 6.750, 30.072, 4.112 x, y, z centers for *Candida glabrata* dihydrofolate reductase complexed with NADPH and 6-methyl-5-[3-methyl-3-(3,4,5-trimethoxyphenyl)but-1-yn-1-yl]pyrimidine-2,4-diamine (UCP115A) (PDB: 3QLY) and 5.942, −16.190, −10.398 x, y, z centers for the thioredoxin reductase from *Entamoeba histolytica* with NADP (PDB ID: 4CCQ). The resulting protein-ligand complexes were analyzed using BioVia Discovery Studio Software to visualize hydrogen bonds, hydrophobic interactions, π-π stacking, and other non-covalent interactions critical for binding stability. Molecular docking scores, which reflect the fit of the ligands into the active sites of target proteins and the predicted strength of the interactions, are presented in Fig. 10–18. These scores provide important information about binding affinity and interaction effectiveness.

3. Results and discussion

3.1. Chemistry

Many derivatives of metronidazole (**3**) may be synthesis because it has functional groups such OH and NO_2. Among these groups, the OH group is the first to be considered as it can undergo both displacement and oxidation reactions. Molecule **4** is a benzene derivative with electron-withdrawing two CN and one NO_2 groups, and it is known to give nucleophilic aromatic substitution reactions [36–39]. NMR, HRMS and FTIR spectra of the synthesized molecule **5** is given in supporting information Fig.1–4.

To synthesize molecule **5**, reaction of **3** and **4** was carried out in basic (with K_2CO_3) media (Scheme 1). As a result of this reaction, molecule **5** was obtained in 65 % yield. The appearance of the NMR spectra of molecule **5** is expected to be similar to those of **3** and **4** overall, except for the chemical shifts and the OH peak. These peaks are really similar. The NMR spectra and HRMS value of molecule **5** are in agreement with the proposed structure.

One of the most important reactions of aromatic molecules are electrophilic aromatic substitutions, especially brominations, in their ring carbons [40]. A molecule containing a NO_2 in the benzene ring of climbazole (**6**) was considered. This molecule **7** may also be more biologically active than **6**. From activating ether and deactivating Cl groups at the para (*p*) positons of benzene ring in **6**, the ether group is more effective in directing and more sensitive to acid. Considering these properties of **6**, the reaction of **6** with HNO_3/H_2SO_4 mixture was performed under mild conditions (ambient tempreture and low concentrations) (Scheme 2). The crude product **7** obtained as a result of washing the reaction mixture with cold $NaHCO_3$ and brine solutions was purified by silica gel column chromatography and crystallization. Only, molecule **7** was isolated from reaction mixture.

When the product was examined in the ^{1}HNMR spectrum of **7**, it was determined that the 4 benzene ring hydrogens, which were equal in pairs in reactant **6**, were transformed into **3** different hydrogens in product molecule **7**. Nine lines observed in the aromatic region of ^{13}CNMR spectrum of **7** should belong to carbon atoms of imidazole and benzene rings because a similar situation is also in the benzene ring carbons in **6** and **7**. Therefore, the NMR and HRMS spectra of product **7** are in agreement with the corresponding structure. Additionally, the structure of **7** was also confirmed by its X-ray analysis (Fig. 2). NMR, HRMS and FTIR spectra of the synthesized molecule **7** is given in supporting information Fig.5–8.

3.2. Crystal strcucture analysis of 7

The molecule **7** was crystallized from different solvents to obtain good quality a single crystals. The crystal structure of **7** was solved and refined in the monoclinic space group $P2_1/n$. According to the SCXRD analysis, the asymmetric unit contains one molecule **7**. In the crystal, the molecule is observed to adopt such a conformation that the imidazole ring is inclined at an angle 80.2° to the aromatic ring and at an angle of 56.2° to the plane of the 3,3-dimethyl-2-butanone fragment. There are no strong intermolecular interactions in the crystal structure. The structure is racemic and the two enantiomers have crystallized together and the two enantiomers are stacked on top of each other in opposite directions with the phenyl-Cl planes parallel to each other (Fig. 2). Here, the O3···C6 [3.151(3) Å] and O4···C4 [3.052(3) Å] atoms are particularly close to each other. Both distances are smaller than the sum of the vdW radii of the oxygen and carbon atoms (3.22 Å). These dimeric groups come together with a weak C7-H···N1^i 3.527(3) Å (i; 1/2-x,1/2*y*,1/2-z) hydrogen bond to form a one dimensional polymeric structure. Again, in Fig. 3, different crystal motifs of the structure are seen along different diagonal axes. The racemic nature of the structure causes the formation of such motifs and patterns. The π-π stacking interactions between the delocalized π-electrons of the phenyl and heterocyclic imidazole rings are weak. The distance between the ring centroids is in the range of 4.35–5.32 Å. However, vdW interactions contribute to the formation of a stable structure.

Table 3 shows the comparative geometric parameters of molecule **7** and molecule **CBZ** (**6**). Theoretical calculated parameters of molecule **7** are also included in the same table. X-ray analysis of the **CBZ** (**6**) molecule was performed at 150 K. The bond lengths in the two structures are particularly close to each other. Because of the nitro unit, the chlorophenyl rings are significantly twisted relative to each other. Structure of **7** is also racemic like that of **CBZ** (**6**) [41].

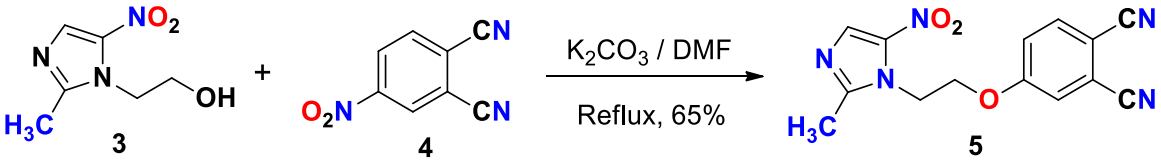

Scheme 1. Synthesis of molecule **5**.

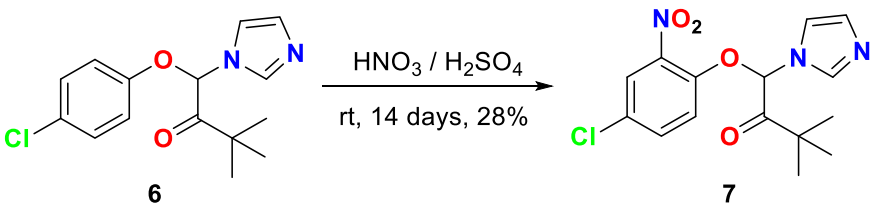

Scheme 2. Synthesis of molecule **7**.

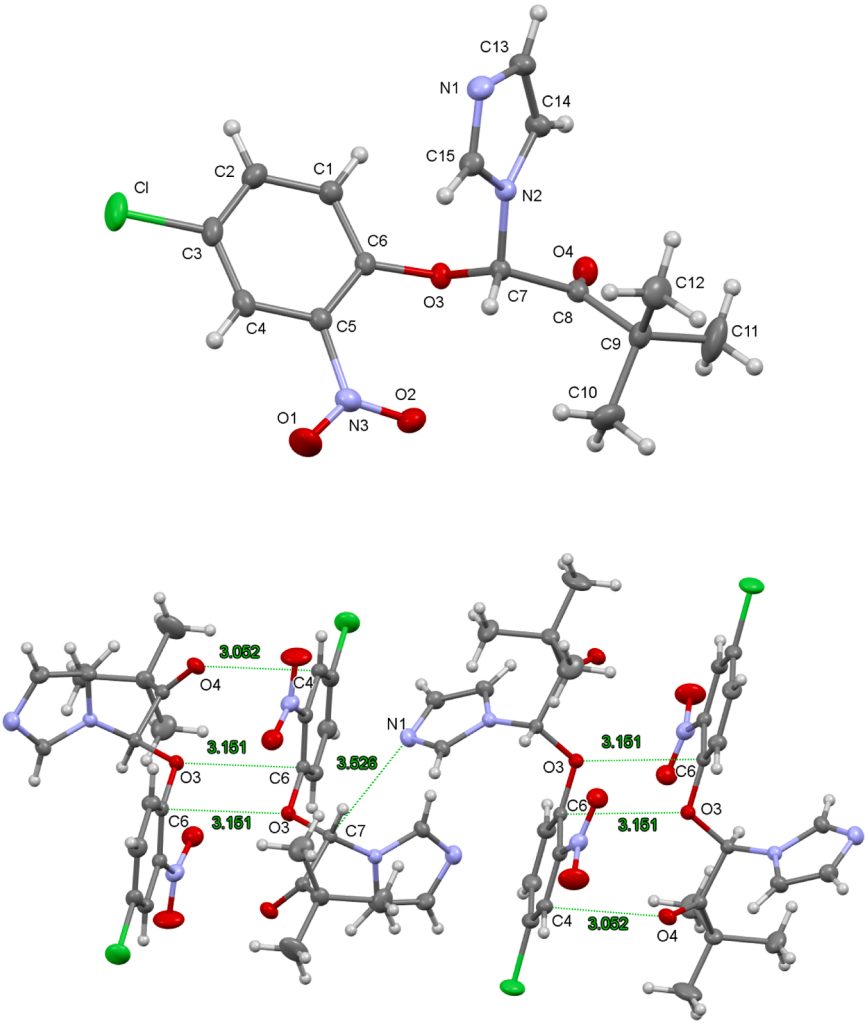

Fig. 2. (Top) ORTEP view of the molecule **7** showing the displacement ellipsoids at 40% probability. (bottom) Short contacts (O3···C6, O4···C4) and the C—H···N interactions between the enantiomers.

3.3. Computational studies

3.3.1. Hirshfeld surface analysis

The Hirshfeld surface analysis [9,28] of the molecule **7** with the CIF file was performed to understand the individual contribution of intermolecular interactions in the crystal. This analysis was carried out using the CrystalExplorer program [42]. The Hirshfeld surface and fingerprint plot of molecule **7** (based on the distance from the surface to the nearest external atom) were generated using [9] and are presented in Fig. 4. Bright red regions on the Hirshfeld surface correspond to O–H•••N hydrogen bonding interactions, while light red hues on the surface indicate C2•••O3 intermolecular interactions. Light yellow patches indicate the presence of short or weak intermolecular C–H•••O interactions. Strong H•••H interactions are represented in blue. Fingerprint analysis of **7** was performed and the results are shown in Fig. 5. The percentage contributions of these interactions were evaluated by fingerprint analysis, and O•••H interactions constitute 20.1 % of the total Hirshfeld surface, H•••H interactions constitute 36.7 %, and Cl•••H interactions constitute 12.8 % (Fig. 5).

The displayed histograms show a portion of the colored dots, with blue dots representing distant contacts and red dots representing significant close contacts. The presence of sharp peaks in regions with low de and di values indicates the strongest intermolecular interactions. Stratification of the total histograms revealed that the contacts providing structural stability to molecule **7** in the unit cells occur at 36.7 % H····H %, 20.1 % H····O/O···H, 12.9 % H····Cl/Cl····H, and 5.1 % C····O, respectively. These data indicate that the primary contacts in both analysis samples are the H····H and H·····O/···H hydrogen bonds, which are the strongest and most intense compared to other intermolecular interactions.

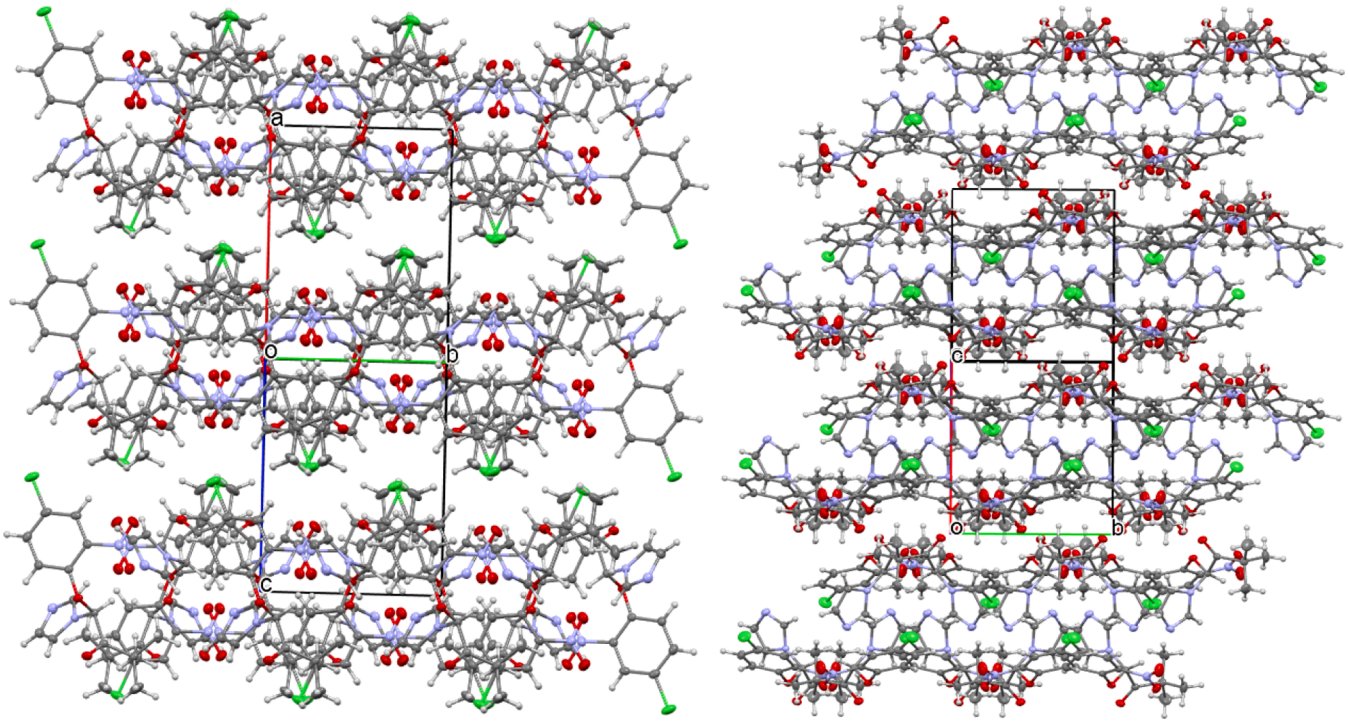

Fig. 3. Crystal lattice motifs of molecule **7** along different diagonal axes.

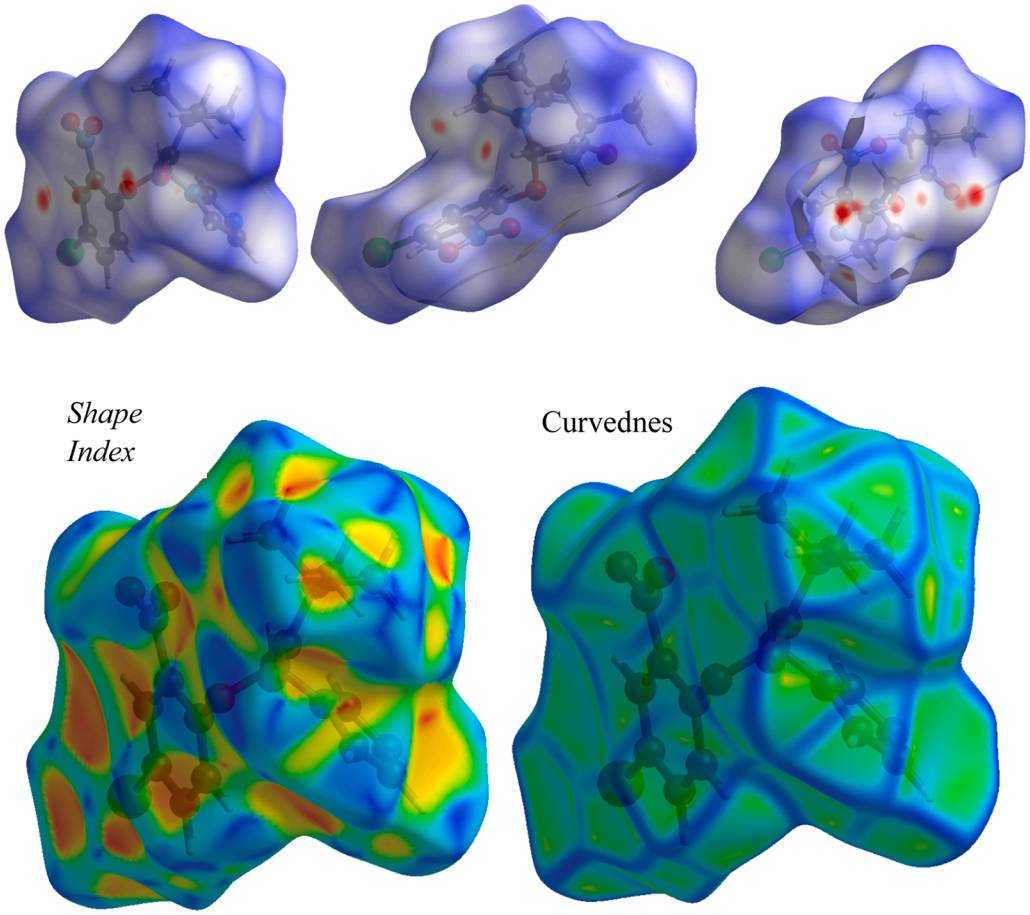

Fig. 4. Two views of the Hirshfeld surface of molecule **7** showing: the surface rendered as d_{norm}, highlighting close contacts of the form C7-H···N1^{i} 3.527(3) Å (i; 1/2-x,1/2 + y,1/2-z) as small red spots; the surface rendered by 'shape index', which provides evidence of π–π stacking as opposing blue and red roughly triangular regions at each of the imidazole and benzene rings and curvedness.

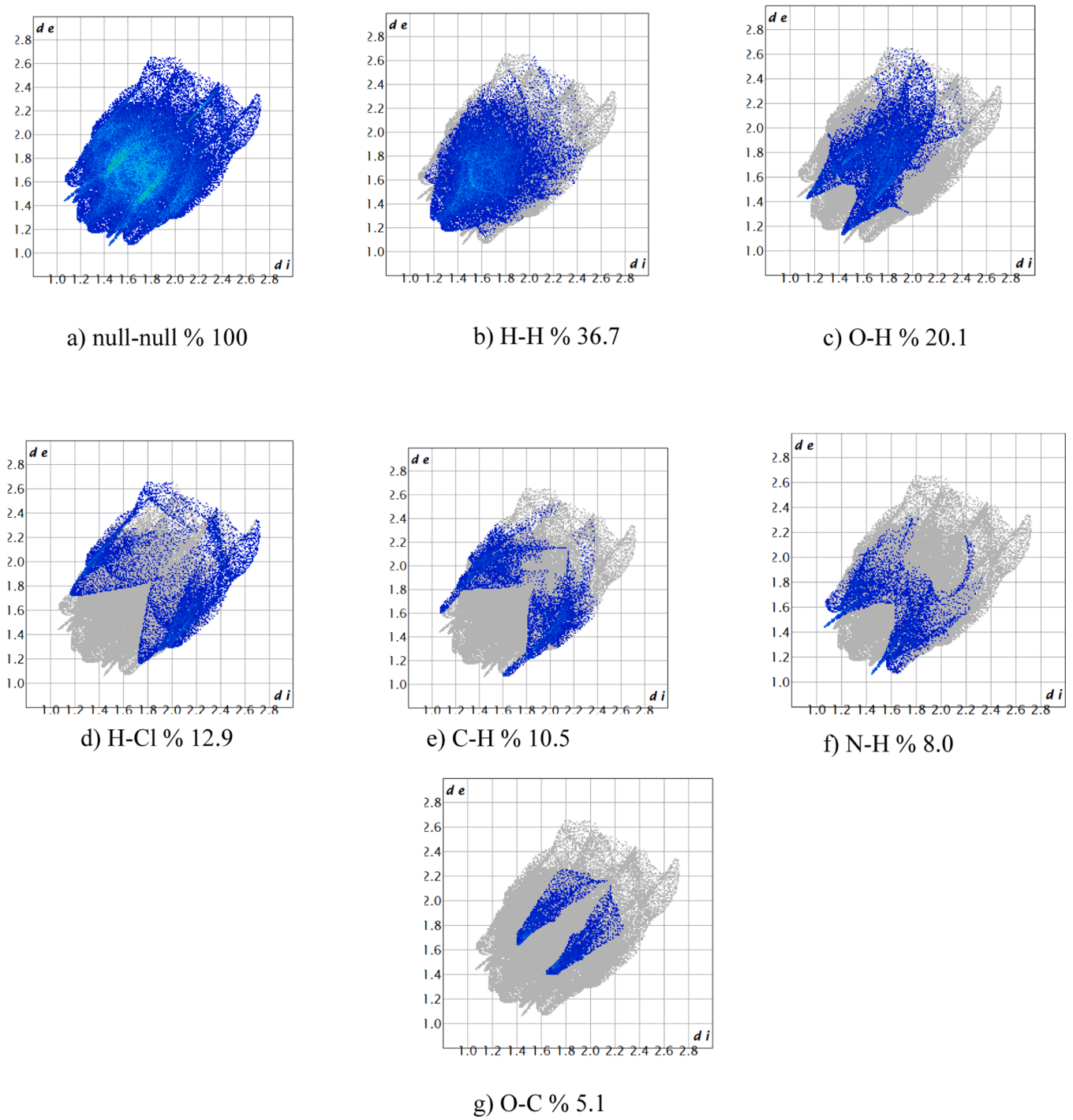

Fig. 5. Two-dimensional fingerprint plots quantifying the various atom–atom contact coverages present in the crystal packing: (*a*) all interactions, and delineated into (*b*) H···*H* = 36.7 %; (*c*) H···O/O···*H* = 20.1 %; (*d*) H···Cl/Cl···*H* = 12.9 %; (*e*) C···*H* = 10.5 %; (f) N···*H* = 8.0 %; (g) O···*C* = 5.1 %… The d_i and d_e values are the closest internal and external distances (in Å) from given points on the Hirshfeld surface.

To better visualize and verify the intermolecular contacts throughout the crystal structure, Hirshfeld surface analysis was performed, supplemented by complementary analyses such as shape index and curvature surfaces.

According to the analysis, the interactions with the largest surface contribution in the crystal structure are H···H contacts. These interactions constitute 36.7 % of the total surface area, making them the most prevalent interaction type in the crystal. This demonstrates the dominance of van der Waals interactions in molecular crystals. The fingerprint plot of H···H interactions (Fig. 5b) exhibits a broad and diffuse distribution near the center; this pattern suggests that these contacts are weak interactions spanning a wide distance range rather than being directional.

The primary factors contributing to the stability of the crystal packing are O···H/H···O hydrogen bonds. These interactions constitute 20.1 % of the total surface area. Their strong and directional nature is observed in the fingerprint plot (Fig. 5c) as sharp and intense peaks at lower values of di and de (internal and external contact distances). This confirms that O····H/H···O hydrogen bonds play a critical role in the orderly arrangement of molecules within the crystal [43,44].

In addition, H···Cl/Cl···H (12.9 %) and C—H (10.5 %) interactions also play an important role in the crystal structure. H···Cl interactions are associated with weak bonds formed between chlorine and hydrogen atoms on the molecule's surface [45]. C—H interactions, on the other hand, involve weak hydrogen bonds such as C—H···O and C—H···π and serve as secondary interactions that support the overall stability of the crystal structure. Other interactions with lower percentage contributions include N—H (8.0 %) and O—C (5.1 %). Each interaction displays a characteristic fingerprint pattern in Hirshfeld surface analysis, providing a comprehensive interaction map of the crystal structure.

As a result, the molecule's crystal structure is largely shaped by H····H and strong O····H/H···O hydrogen bonds. These dominant interactions, supplemented by weaker interactions such as H····Cl/Cl···H, C–H, and N–H, determine the overall stability and morphology of the crystal.

3.3.1.1. Energy frameworks. Energy framework analysis, performed to better understand the stability of the crystal structure and the arrangement of molecules in the solid state, is an effective approach for visualizing intermolecular interaction energies [46]. The pairwise interaction energy calculations carried out using the CE-B3LYP model provided a detailed representation of the energy framework of the crystal structure.

The different colored cylinders shown in Fig. 6, which connect the molecules, visualize the main interactions responsible for the formation of the crystal lattice. This energy component often plays a decisive role in the stability of the crystal structure. The red cylinders correspond to electrostatic interactions between molecules, while the blue ones represent the total interaction energy and yellow cylinders destabilizing interactions [46]. The pronounced dominance of dispersion energies clearly demonstrates that the ordering of the crystal structure is largely governed by the close packing of atoms. This finding confirms that the experimentally observed crystal structure is stabilized not by strong and directional bonds, but rather by a complex network of weak and non-directional interactions [47].

These data clearly demonstrate the decisive influence of the dispersion energies on three different orientations of the crystal structure. The energy framework was analyzed to better understand the packing, topology, and supramolecular rearrangement of the crystal structure (Fig. 6). It is concluded that the formation of the energy framework, relative to the tube orientation, is driven by the translational symmetry elements and the central symmetry setting of the crystal. This rearrangement allows other weak interactions to form in the crystal structure. Calculations show that dispersion interactions create approximately complex hexagonal energy topologies in the crystal. The lower values of the electrostatic energy compared to the dispersion energy in all three molecules are attributed to the absence or very low presence of classical hydrogen bonding interactions. However, numerous weak interactions are present in the crystal packing.

3.3.2. DFT studies

3.3.2.1. Geometry optimization. The optimized structure of molecule **7** in the gas phase was calculated by DFT at the theoretical level RmPW1PW91/6–311G(d,p) using the Gauss 09 W program [30]. The optimization results were visualized by GaussView 5.0; the optimized structure (Fig. 7), HOMO and LUMO orbitals (Fig. 8) and the Molecular Electrostatic Potential (MEP) surface (Fig. 9) were generated. The structure obtained as a result of the optimization shows that the piperidine ring of (I) has a distorted boat conformation in the gas phase; this finding is consistent with the data obtained from solid state SC-XRD study. Comparison of the theoretically calculated bond parameters and the values obtained from diffraction analysis reveals the high consistency between them (Table 3). In addition, the geometry of the low-temperature crystal structure of metronidazole was determined [48] is largely similar to the room temperature structure reported [49]. The main interactions that stabilize the crystal structure of the metronidazole molecule include O–H···N hydrogen bonding and C–H···O intramolecular and intermolecular interactions.

A comprehensive comparison of geometric parameters derived from density functional theory (DFT) calculations with experimental data obtained [49] shows remarkable agreement, particularly for bond lengths and many bond angles. This consistency confirms that the applied DFT methodology successfully predicts the molecular geometry of the molecule of interest. Because theoretical calculations are typically based on isolated molecules in the gas phase, while experimental measurements include environmental influences such as crystal packing, the small deviations observed are within expected limits (e.g., approximately 0.01–0.03 Å for bond lengths and 1–3° for bond angles), a phenomenon consistently reported in the literature [50].

The atomic numbers indicated in Table 2 are prepared according to the numbering specified in the optimized structure of molecule **5**. In detailed analysis, a clear similarity was observed in the bond lengths of ~~(~~C1–N4 (experimental: 1.351(2) Å; DFT: 1.3622 Å) and (C1–N6) (experimental: 1.334(2) Å; DFT: 1.3217 Å) with very small differences of about 0.01 Å. All other bond lengths, including (C1–C7), (C2–C3), (C2–N6), (C3–N4), (C3–N31), (N4–C11), (C11–C14), (C14–O17), (N31–O32), and (N31–O33), also exhibit excellent agreement between

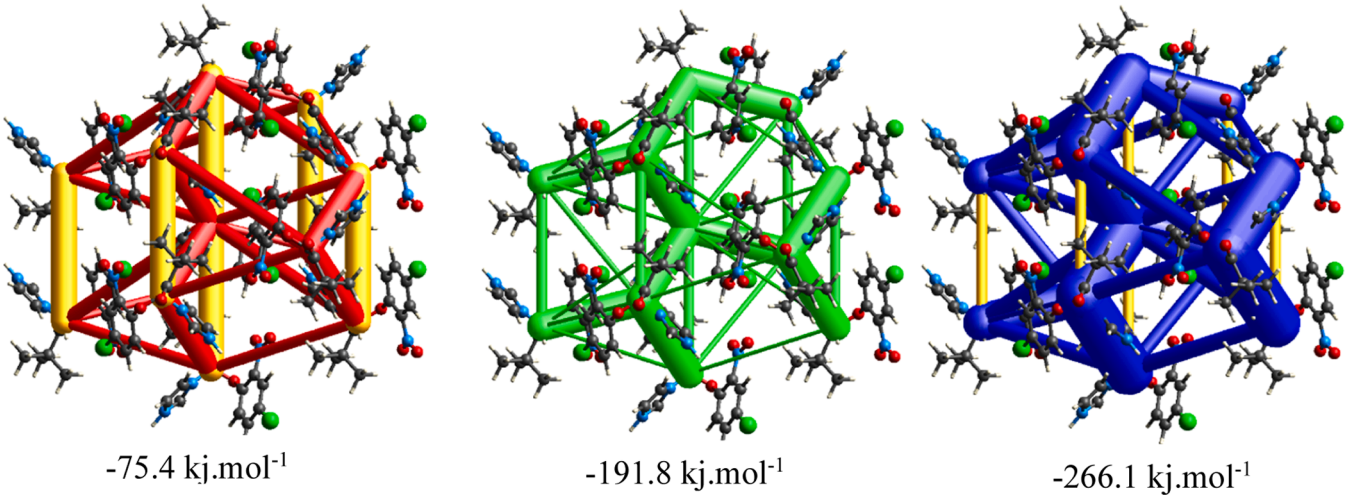

Fig. 6. Energy framework diagrams for electrostatic (red) and dispersion (green) contributions to the total interaction energies (blue) and destabilizing interactions (yellow). The cylindrical radii are proportional to the relative strength of the corresponding energies.

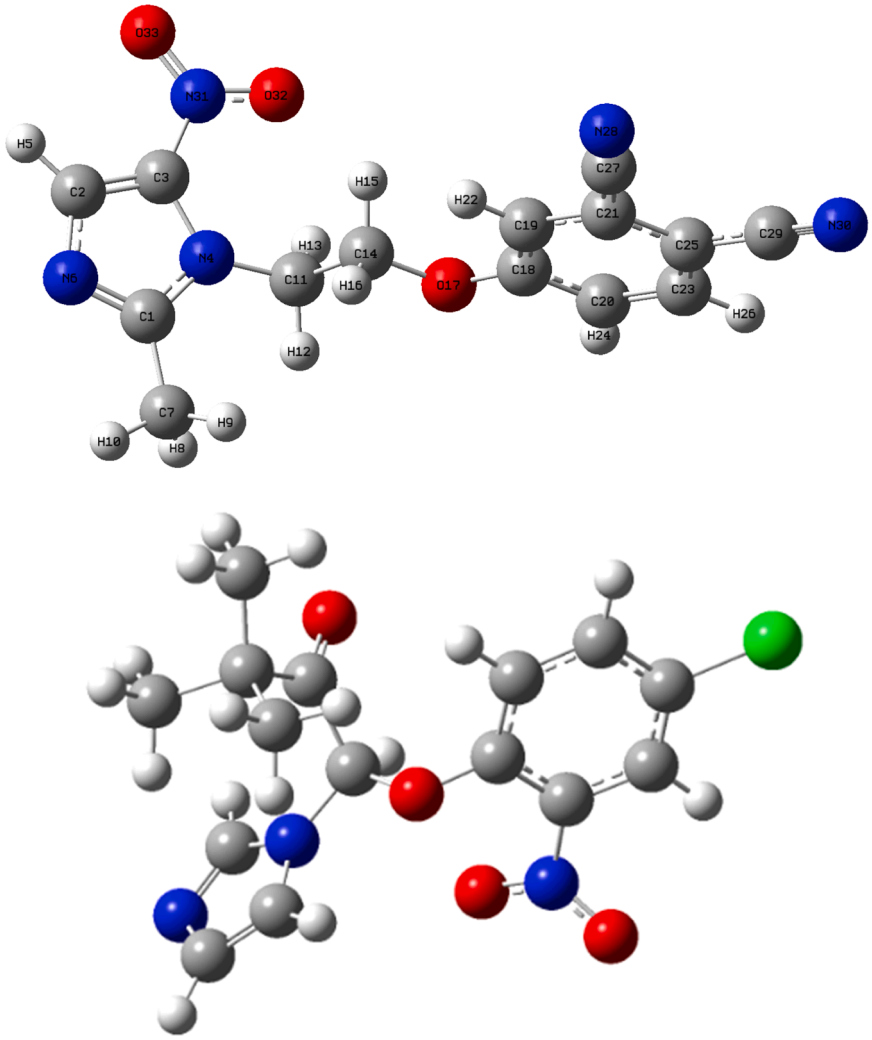

Fig. 7. DFT optimized structure of **5** (top) and **7** (bottom).

DFT and experimental data. Furthermore, DFT calculations for bonds such as (C2–H5), (O17–C18), (C27–N28), and (C29–N30), for which experimental data are not available, provide valuable theoretical predictions for structural analysis. In terms of bond angles, there is also strong consistency between experimental and theoretical results, as for example A(N4–C1–N6) (experimental: 111.5(1)°; DFT: 112.157°); the difference in this example is <1° Other angles, such as (N6–C1–C7), (C3–C2–N6), (C2–C3–N4), (C2–C3–N31), (N4–C3–N31), (C1–N4–C3), (C1–N4–C11), (C3–N4–C11), (C1–N6–C2), (N4–C11–C14), (C11–C14–O17), (C3–N31–O32), (C3–N31–O33), and (O32–N31–O33), also show very close similarities. Angles containing hydrogen atoms (e.g., (C3–C2–H5)) may deviate by a few degrees due to the difficulties in precise experimental positioning and the higher sensitivity of theoretical calculations to these atoms; nevertheless, the general agreement is preserved. Additionally, the lack of experimental data for some angles, such as (C14–O17–C18), (O17–C18–C19), and (O17–C18–C20), makes DFT calculations the primary source of information for these structural parameters. All DFT calculated data of molecule **5** given in ***SI-*** Table 1.

Dihedral angles, which define the rotation about a bond, can vary more between experimental and theoretical methods, especially in flexible regions of the molecule. "L"-type angles such as (C21–C27–N28–C25–1) have only been obtained by DFT calculations, suggesting that these values are either not reported experimentally or are difficult to determine. These DFT-based angles are generally close to 180°, indicating that the structures have a nearly planar or anti-periplanar conformation. Excellent agreement was observed for dihedral angles such as (N4–C3–N31–O32) (experimental: –3.4(3)°; DFT: –4.153°) and (N4–C3–N31–O33) (experimental: 176.1(2)°; DFT: 176.14°). The (C3–N4–C11–C14) angle (experimental: 82.6(2)°; DFT: 82.236°) shows that both methods agree on a significant non-planar torsion. In contrast, there is a remarkable discrepancy in the (N4–C11–C14–O17) dihedral angle: the experimental value is 61.2°, while the DFT value is 175.394° This large discrepancy may be due to the differences between the conformation in the crystal structure (solid state) and the optimized structure in the gas phase. Environmental factors, especially crystal packing effects, cannot be taken into account in isolated molecule models, which may lead to the observed deviations.

In conclusion, DFT calculations generally accurately represent the molecular geometry of molecules like Metronidazole (**3**), providing a high level of agreement between experimental data and most bond lengths and angles. While small deviations are considered normal in such comparisons, significant differences in specific dihedral angles, such as (N4–C11–C14–O17), suggest the possibility of conformational flexibility in the molecule and that crystal forces may stabilize a conformation different from the gas-phase structure. Such discrepancies highlight the need for further research to understand the role of environmental influences on molecular structure.

*3.3.2.2. Electronic properties and comparison of molecule **5** and molecule **7***

Building upon the structural analysis, we next investigated the electronic properties of molecule **5**, a stable derivative with potential biological activity. This molecule, 4-(3-(2-methyl-5-nitro-1*H*-imidazol-

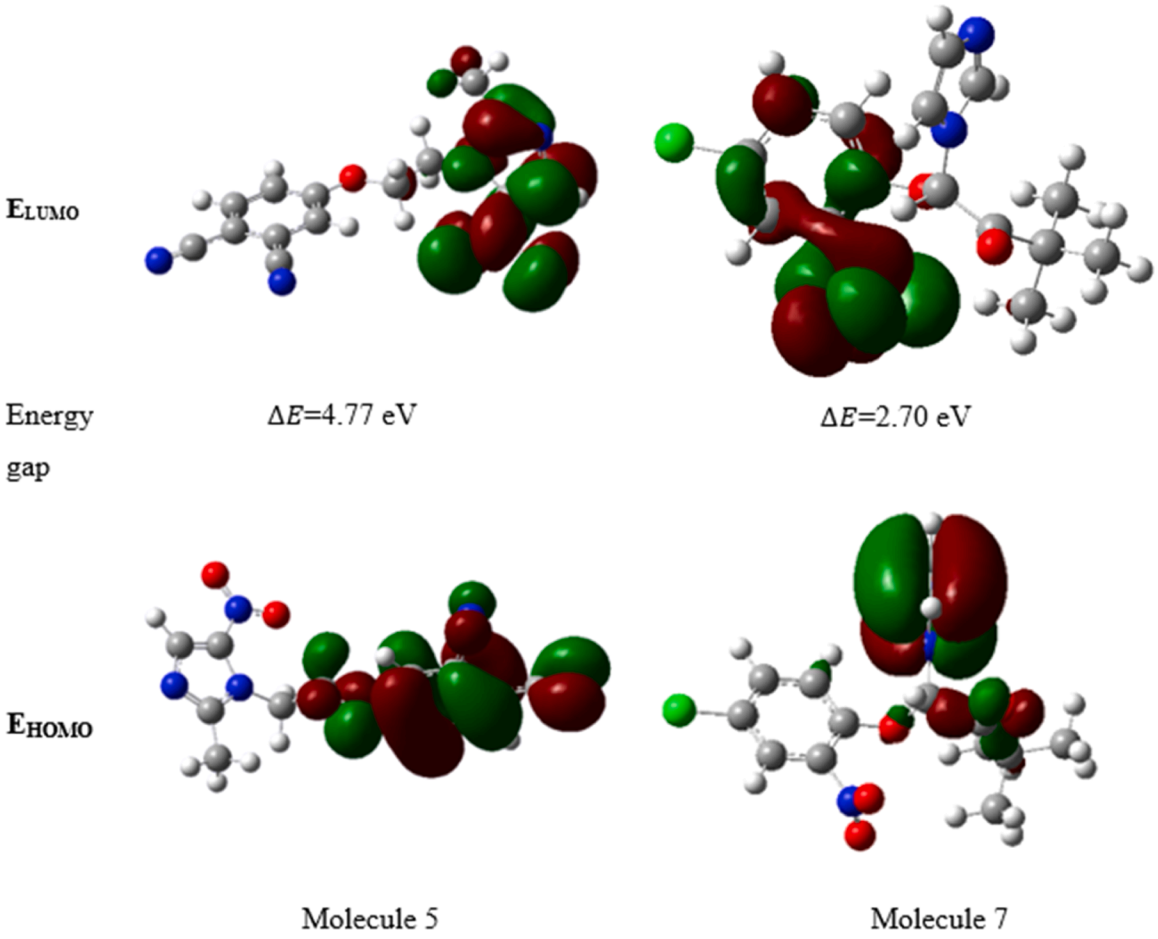

Fig. 8. Energy distributions and differences of the HOMO and LUMO molecular orbitals for molecules **5** and **7**, calculated using Density Functional Theory (DFT) with the mPW1PW91/6–311G(d,p) and wb97xd/6–311G(d,p) basis sets, respectively.

1-yl)propyl)phthalonitrile, (**5**) was designed and synthesized by adding a new functional group to the basic structure of metronidazole, and its antibacterial and antifungal activities were investigated by in silico methods, characterized by NMR and HRMS spectra. The electronic properties of molecule **5** (such as polarity and stability) provide important structural and functional information.

For comparative analysis, the electronic properties of molecule **5** are herein compared with molecule **7**, which serves as a representative metronidazole derivative in this study. The electronic energy of molecule **5** (–1506.383461 Hartree) is significantly lower compared to molecule **7** (–1039.394087 Hartree). This lower electronic energy indicates that molecule **5** has a more thermodynamically stable structure. This finding demonstrates that the addition of the phthalonitrile group contributes positively to molecular stability. Furthermore, the dipole moment of molecule **5** (5.429169 Debye) is lower than that of molecule **7** (8.625415 Debye). This suggests that molecule **5** is less polar, and the phthalonitrile group reduces the overall molecular polarity. This difference suggests that the phthalonitrile group provides a more nonpolar electronic environment compared to other structures derived from the metronidazole nucleus. This comparative analysis clearly demonstrates that the addition of a functional group to molecule **5** increases the molecule's stability while decreasing its polarity. These changes in electronic properties may have significant effects on the molecule's biological activity, intracellular penetration, and interaction profile with target biomolecules.

Table 3 presents a comparative analysis of selected bond distances, bond angles, and torsional angles for the molecule **7** derived from both experimental (X-ray crystallography for **7** and **6** [41] and theoretical (DFT) calculations. This comparison provides important information about the accuracy of the DFT method in predicting molecular geometries and highlights possible conformational differences between the gas-phase optimized structure and the solid-state experimental data.

The bond lengths calculated by the DFT method for molecule **7** are in very good agreement with the experimental data obtained for the molecule **7**. Most of the calculated bond lengths, e.g., Cl-C3 (DFT: 1.739 Å; experimental: 1.735(3) Å), O3-C6 (DFT: 1.3737 Å; experimental: 1.375(3) Å), O3-C7 (DFT: 1.4185 Å; experimental: 1.424(3) Å), and C8-O4 (DFT: 1.2038 Å; experimental: 1.204 Å), are remarkably close to their experimental counterparts and lie within the reported experimental error limits. This agreement highlights the reliability of the DFT method in accurately reproducing the local molecular geometry, a finding well known in the computational chemistry literature [51]. Comparisons with **6** [41] also show strong overall consistency, demonstrating that the basic skeletal structure and interatomic bonds of the molecule are quite stable and unchanged even under different phase conditions (gas phase and solid state).

As with the bond lengths, many bond angles calculated by DFT also show good agreement with the experimental data. For example, the C6–O3–C7 angle was calculated as 114.7674°, which is quite close to the experimental **7** value of 115.18° However, some angles show more significant deviations: for example, the O3–C7–C8 angle was calculated as 112.8394° by DFT, while its experimental value is 105.45°; similarly, the calculated value for the C7–C8–C9 angle was 114.7674°, while its experimental value was 118.64° These angles show deviations of approximately 7° and 4°, respectively. Such differences indicate inherent differences between the optimized structures in the gas phase

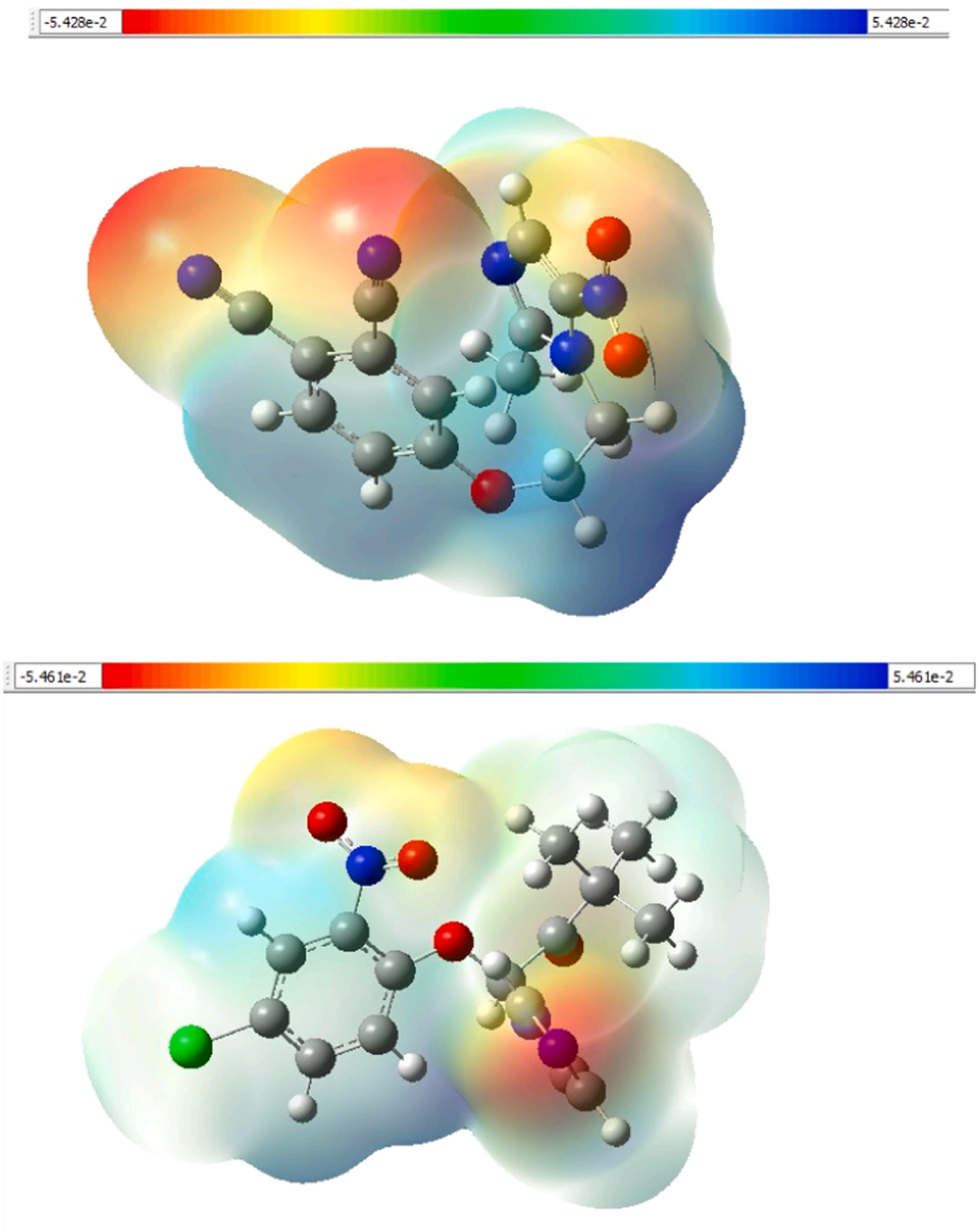

Fig. 9. Molecular electrostatic potential surface of **5 (up)** and **7 (down)**.

(DFT calculations) and the X-ray crystallography data obtained in the solid state. Crystal packing forces, in particular, may influence the local geometry of the molecule. Therefore, these deviations may indicate a certain flexibility in the angular arrangements in some regions of the molecule, depending on external environmental influences. This flexibility suggests that the molecule may affect its interactions with neighboring molecules in the crystalline environment [21].

The most significant differences between the theoretical and experimental structures are observed in the torsion angles, which are highly sensitive to molecular conformation and flexibility. For example, the torsion angle for O3–C6–C5–N3 was calculated by DFT as −1.99°, which is in excellent agreement with the experimental value of −2.34° In contrast, the DFT value for N2–C7–C8–O4 was 77.40°, while the experimental angle was −84.16° Similarly, the DFT value for N2–C7–C8–C9 was −96.87°, while the experimental angle was 95.43° This indicates significant deviations of approximately 161° and 192° in the respective torsion angles, respectively. These significant differences in torsion angles indicate a significant conformational difference between the structure optimized in the gas phase (DFT) and the solid-state structure determined by X-ray diffraction in the crystal environment. These differences are generally attributed to crystal packing forces -weak intermolecular forces such as hydrogen bonds and van der Waals interactions- which can force the molecule into a structure different from its lowest-energy conformation in the solid state (in the gas phase) than its preferred conformation in isolation [50]. Therefore, theoretical calculations provide information about the intrinsically preferred conformation of molecule **7** in the free state (in the gas phase), independent of crystal lattice effects. These large differences in torsion angles clearly demonstrate that molecule **7** is highly conformationally flexible, and that packing forces in the crystal environment can suppress this flexibility and stabilize a different conformation. This conformational flexibility is critical to the molecule's ability to interact with

Table 2
Selected bond distances, bond angles and torsion angles (Å, °) of **MTZ** (**3**) and theoretical (DFT) calculations of molecule **5.**

	3 [39]	DFT (5)
C1-N4	1.351 (2)	1.3622
C1-N6	1.334 (2)	1.3217
C1-C7	1.479 (2)	1.4847
C2-C3	1.356 (2)	1.3714
C2-H5	—	1.0775
C2-N6	1.359 (2)	1.3503
C3-N4	1.383 (2)	1.3842
C3-N31	1.414 (2)	1.4181
N4-C11	1.475 (2)	1.454
C11-C14	1.510 (2)	1.5192
C14-O17	1.410 (2)	1.4174
O17-C18	—	1.3458
C27-N28	—	1.1526
C29-N30	—	1.1531
N31-O32	1.226 (2)	1.226
N31-O33	1.221 (2)	1.214
N4-C1-N6	111.5 (1)	112.157
C2-C3-N31	126.9 (1)	127.951
C1-N4-C11	125.5 (1)	125.508
C11-C14-O17	112.4 (1)	105.497
C14-O17-C18	—	118.991
O17-C18-C19	—	124.232
C3-N31-O33	116.6 (1)	116.869
O32-N31-O33	123.3 (1)	124.918
C21-C27-N28-C25	—	181.611
C25-C29-N30-C21	—	181.516
C21-C27-N28-C25	—	180.337
C25-C29-N30-C21	—	179.804
N4-C3-N31-O32)	–3.4 (3)	−4.153
N4-C3-N31-O33)	176.1(2)	176.14
C3-N4-C11-C14)	82.6 (2)	82.236
N4-C11-C14-O17)	61.2	175.394

Table 3
Selected bond distances, bond angles and torsion angles (Å) of CBZ (**6**) and **7** with theoretical (DFT) calculations of molecule **7**.

	7	6 [41]	DFT (7)
Cl-C3	1.735(3)	1.742(2)	1.739
O3-C6	1.375(3)	1.388(2)	1.3737
O3-C7	1.424(3)	1.418(2)	1.4185
C7-N2	1.450(3)	1.448(2)	1.452
N2-C14	1.372(3)	1.379(2)	1.3764
N2-C15	1.357(3)	1.358(2)	1.3683
N1-C15	1.309(3)	1.311(2)	1.3029
N1-C13	1.370(3)	1.377(2)	1.3727
C7-C8	1.544	1.548(2)	1.5553
C8-O4	1.204	1.205(2)	1.2038
N3-C5	1.447		1.4713
N3-O1	1.217		1.2111
C6-O3-C7	115.18(3)	118.13(2)	114.76
O3-C7-C8	105.45(3)	102.94(2)	112.84
C7-C8-C9	118.64(3)	116.68(2)	114.77
C6-O3-C7-N2	−65.64(3)	−79.84/2)	−80.07
N2-C7-C8-O4	−84.16(3)	−35.27(2)	77.40
N2-C7-C8-C9	95.43(3)	144.24(2)	−96.86
O3-C6-C5-N3	−2.34(3)		−1.99

biological targets or other chemical species.

3.3.2.3. Computational details and results

Understanding molecular structures and properties is a fundamental step for predicting their behavior in chemical and biological systems. Density Functional Theory (DFT) is a powerful and widely used computational chemistry method for investigating the electronic structure and thermodynamic properties of molecular systems [52,53]. In this study, the optimized geometries, electronic, frontier molecular orbital (FMO), electrostatic potential (ESP), and thermodynamic properties of molecules **5** and **7** were comparatively investigated using the DFT approach.

All geometric optimizations and frequency analyses were performed using Gaussian software on multi-core systems, with visualization via GaussView 6 [https://gaussian.com/wp-content/uploads/dl/gv6.pdf]. For both molecules, a charge of 0 and a singlet spin state were assumed, and solvent effects were neglected. The absence of imaginary frequencies in all optimized structures confirmed that they correspond to true minima on the potential energy surface, a fundamental criterion for structural stability [51].

Geometry optimizations for molecule **7** were performed using the RmPW1PW91 functional and the 6–311G(d,p) basis set. The convergence criterion was set to an RMS gradient norm of 0.000006 Hartree/Bohr, and the optimization was successfully completed in a single step. The maximum force value was calculated as 0.000016, the RMS force as 0.000003, the maximum displacement as 0.001070, and the RMS displacement as 0.000199 Bohr. Similarly, the geometry optimization for molecule **5** was conducted using the RwB97XD functional and the same basis set as 6–311G(d,p). The RMS gradient norm was set as 0.000007 Hartree/Bohr, and the optimization for this molecule was also completed in a single step. The maximum force value was obtained as 0.000019, RMS force as 0.000004, maximum displacement as 0.002366, and RMS displacement as 0.000593 Bohr.

The use of different functionals for molecule **5** and molecule **7** stems from the need to optimize computational accuracy for the specific chemical properties or interactions dominant in each molecule, ensuring the most reliable results for their distinct characteristics. For Molecule **7**, being a halogenated crystalline molecule, the wb97xd functional with its empirical dispersion corrections is particularly important for accurately modeling intermolecular interactions within its crystal structure.

3.3.2.4. Comparison of electronic properties. The electronic energy, dipole moment, and polarizability values for both molecules are summarized in Table 4.

The electronic energy of molecule **7** was found to be −1039.394087 Hartree (−28,351.48 eV), while that of molecule **5** was −1506.383461 Hartree (−40,997.10 eV). This difference arises from the varying atomic numbers and electronic structures of the molecules. Molecule **7** exhibits a significantly higher dipole moment (8.625415 Debye) compared to molecule **5** (5.429169 Debye), indicating a more polar character for molecule **7** and thus potentially more pronounced electrostatic interactions in intermolecular processes [54]. Polarizability, which describes a molecule's ease of electron distribution distortion in response to an external electric field, was calculated as 195.235000 a.u. for molecule **7** and 199.784333 a.u. for molecule **5**, a crucial parameter in fields such as non-linear optics [55].

3.3.2.5. Comparison of frontier molecular orbitals (FMO). Frontier molecular orbitals (HOMO and LUMO) are critically important for understanding a molecule's chemical reactivity [56,57]. The chemical, optical, and electronic characteristics of molecules are largely determined by these frontier orbitals. Specifically, the Highest Occupied Molecular Orbital (HOMO) and the Lowest Unoccupied Molecular Orbital (LUMO) play pivotal roles in understanding molecular reactivity and electronic transitions [58]. The energy gap between the HOMO and LUMO (HOMO-LUMO gap) is a crucial parameter reflecting molecular

Table 4
Comparison of electronic properties for Molecule **7** and Molecule **5.**

Property	Molecule 7	Molecule 5
Electronic Energy	−1039.394087 Hartree (−28,351.48 eV)	−1506.383461 Hartree (−40,997.10 eV)
Dipole Moment	8.625415 Debye	5.429169 Debye
Polarizability (α)	195.235000 a.u.	199.784333 a.u.
Point Group	C1	C1

kinetic stability and chemical reactivity; a smaller gap generally implies higher reactivity and easier electronic excitations, influencing optical properties such as absorption and emission [59]. These frontier orbitals are fundamental in predicting sites for nucleophilic and electrophilic attacks, charge transfer processes, and various spectroscopic behaviors [60], providing critical insights into a molecule's potential applications.

For our molecules, particularly the imidazole-based derivatives like Molecule **5** and the halogenated crystalline molecule **7**, understanding their FMOs through DFT calculations is essential. The DFT optimized structures are shown below in Fig. 7, and their Frontier Molecular Orbital structures are visualized in Fig. 8. Computational studies on similar imidazole derivatives have utilized FMO analysis to elucidate electronic properties and reactivity, often correlating HOMO-LUMO gaps with chemical reactivity and bioactivity [61]. For halogenated crystalline molecules, DFT studies, including FMO analysis, are crucial for understanding their electronic structure, energy gaps, and overall molecular properties, especially considering the influence of halogen and other non-covalent interactions on their crystal packing and reactivity [47,62].

FMO analyses of Molecules **5** and **7** investigated in this study revealed a significant difference between the reactivity profiles of the molecules. The higher energy range of Molecule **5** ($\Delta E = 9.54$ eV) indicates that the molecule is kinetically stable, while the lower energy range of Molecule **7** ($\Delta E = 5.40$ eV) indicates a more reactive structure.

These findings are consistent with other theoretical studies on organic molecules with similar structures. For example, a study on FMO analyses of imidazole derivatives showed that the reactivity of such molecules is directly related to the HOMO-LUMO energy difference, and that their propensity for electrophilic/nucleophilic reactions can be predicted by this parameter [59,61]. The lower energy range of molecule **7** suggests that this molecule is more prone to electron transitions and therefore a more suitable candidate for molecular reactions. This comparison supports our findings on the molecules' reactivity in a scientific context.

The specific FMO values for Molecule **7** and Molecule **5** are presented in Table 5. Molecular surfaces for selected LUMO and HOMO orbitals were visualized at an isovalue of 0.02.

A comparison of the determined frontier orbital energies reveals differences between molecule **7** and molecule **5**. Notably, the LUMO-1 energy of molecule **5** has a positive value, while all other frontier orbital energies for both molecules are negative. The HOMO-LUMO energy gap provides crucial information about a molecule's reactivity and electronic excitation properties; a smaller gap may indicate higher reactivity [56].

To gain a deeper understanding of the electronic reactivity and chemical behaviour of Molecules **5** and **7**, a conceptual DFT analysis was performed based on the HOMO and LUMO energy values, and global reactivity descriptors including electronegativity (χ), chemical hardness (η), softness (σ), chemical potential (μ), and electrophilicity index (ω) were calculated (Table 6). It is widely recognized in the literature that these descriptors provide valuable insights into the nucleophilic/electrophilic character of molecules, their chemical stability, and their overall tendency to undergo chemical reactions [59,61].

Frontier Molecular Orbital (FMO) analysis reveals that the HOMO energy of Molecule **5** (−9.36 eV) is lower than that of Molecule **7**, indicating higher stability and a reduced tendency to donate electrons. In contrast, Molecule **7** exhibits a smaller HOMO–LUMO gap (2.70 eV versus 4.77 eV for Molecule **5**), reflecting higher chemical reactivity and an increased propensity for electron transfer. The LUMO of Molecule **7** highlights potential electron-accepting regions, which, together with its higher electrophilicity index (4.87 eV), suggest an enhanced capability to participate in electrophilic reactions.

Table 5
Frontier molecular orbital (FMO) energies for molecule **7** and molecule **5.**

Molecule	Orbital	Energy (Hartree)	Energy (eV)
Molecule 7	LUMO −1	−0.09594	−2.61
	LUMO	−0.08931	−2.43
	HOMO	−0.28768	−7.83
	HOMO +1	−0.28946	−7.88
Molecule 5	LUMO −1	−0.02672	−0.73
	LUMO	0.00656	0.18
	HOMO	−0.34408	−9.36
	HOMO +1	−0.32179	−8.76

Table 6
The calculated quantum chemical parameters were obtained using the DFT/mPW1PW91/6–311G(d,p) level of theory for Molecule **5** and the DFT/ωB97XD/6–311G(d,p) level of theory for Molecule **7**.

Parameters	Formula	Molecule **5** (eV)	Molecule **7** (eV)
Ionization Potential (I)	$-E_{HOMO}$	9.36	7.83
Electron Affinity (EA)	$-E_{LUMO}$	−0.18	2.43
Chemical Potential (μ)	$(E_{HOMO} + E_{LUMO})/2$	−4.59	−5.13
Global Hardness (η)	$(E_{LUMO} - E_{HOMO})/2$	4.77	2.70
Global Softness (σ)	$1/\eta$	0.21	0.37
Electronegativity (χ)	$-\mu$	4.59	5.13
Electrophilicity (ω)	$\mu 2/(2\eta)$	2.21	4.87

The calculated global reactivity descriptors further support these observations. Molecule 5 shows higher chemical hardness (4.77 eV), indicating that the phthalonitrile group stabilizes its electronic structure and reduces its overall reactivity, making it more resistant to chemical transformations. Conversely, Molecule **7**, with lower hardness and higher softness (0.37 eV^{-1}), is more chemically reactive and prone to electron transfer processes. The negative electron affinity of Molecule **5** further confirms its lower tendency toward electrophilic interactions. Overall, FMO and global reactivity analyses consistently indicate that Molecule **7** is more reactive than Molecule **5**, which may have implications for its potential biological activity and intermolecular interactions, in agreement with trends reported for metronidazole and imidazole derivatives [63,64].

3.3.2.6. Comparison of electrostatic potential (MEP) analysis. Molecular Electrostatic Potential (*MEP*) surfaces are an important tool for visualizing the potential energy distribution around a molecule [57]. *MEP* maps provide insights into a molecule's charge distribution and, consequently, identify potential reactive regions crucial for molecular recognition, hydrogen bonding, and other intermolecular interactions. Red regions typically indicate high negative charge density (electron-rich, nucleophilic character), while blue regions indicate positive charge density (electron-poor, electrophilic character) [65].

MEP maps were generated for both molecules to visualize potential electrophilic and nucleophilic attack regions. For molecule **7**, the *MEP* map indicates intense negative potential primarily on oxygen atoms, while for molecule **5**, the maps similarly reveal the distribution of charged regions. Such maps are crucial for understanding how molecules may interact with biological targets or other chemical species. The Molecular Electrostatic Potential surfaces for both molecules are depicted in Fig. 9.

Molecular electrostatic potential (MEP) analysis was performed to further investigate the electronic environment surrounding the chlorine (Cl) atom in the crystal structure of molecule **7**. The analysis revealed the presence of a positively charged, electron-deficient region (called a σ-hole) along the covalent bond axis of the chlorine atom. This phenomenon results from the anisotropic distribution of electron density around the halogens and leads to a positive electrostatic potential localized in the opposite direction of the covalent bond. It is widely reported in the literature that such σ-holes facilitate the formation of strong, directional interactions known as halogen bonds, which play a significant role in intermolecular interactions [47,66,67].

Studies on similar halogenated molecules indicate that these

σ-vacancy interactions play a critical role in the target-specific interactions of halogen atoms, particularly those found in drug molecules, with proteins and biomolecules [68–70]. The positive potential region around the chlorine atom of molecule **7** suggests that the molecule may act as a halogen bond donor, which may be responsible for its possible biological activity or molecular arrangement in the crystal structure.

3.3.2.7. Comparison of thermodynamic properties. Thermodynamic analyses provide crucial information about the stability of molecules under different conditions and the thermodynamic feasibility of reactions. For both molecules, key thermodynamic parameters were calculated at 298.15 Kelvin and 1 atm pressure, as summarized in Table 7.

These thermodynamic parameters characterize the molecules' thermal mobility, the degree of disorder within the system, and their capacity for energy exchange with their surroundings. For instance, higher entropy values may suggest greater conformational freedom or a higher degree of disorder for a molecule at a given temperature. Here the thermodynamic parameters of molecule **5** are higher than molecule **7.**

DFT frequency analyses performed for Molecules **5** and **7** at 298.15 K and 1000 atm reveal how structural differences in the molecules affect their thermodynamic stability. The resulting thermal energy, enthalpy, heat capacity, and entropy values provide important information about the internal energy and thermodynamic equilibrium of the molecules. Calculating these thermodynamic parameters is a common method for predicting the stability and reactivity of similar organic molecules [63].

The analysis results show that Molecule **5** (E = 203.347 kcal/mol) has higher thermal energy and enthalpy values than Molecule **7** (E = 164.857 kcal/mol). This finding is consistent with Molecule **5** having higher vibrational degrees of freedom due to its larger molecular volume and greater atomic number. Similarly, the higher heat capacity (Cv = 79.871 cal/mol-K) and entropy (S = 156.188 cal/mol-K) values of Molecule 5 indicate that the molecule has greater molecular disorder and freedom of movement.

These findings are consistent with other organic molecules reported in the literature; molecules with more complex and flexible structures are generally known to exhibit higher thermodynamic correction values. These thermodynamic data support the experimental melting point data of the molecules, confirming that Molecule **7** has a more ordered and rigid structure, resulting in stronger crystal packing and, consequently, a higher melting point.

3.3.2.8. Root mean square deviation (RMSD) by pymol. The structural comparison between X-ray structure and DFT was performed for molecule **7** using PyMOL (Schrödinger, LLC) (*SI*-Fig. 9). The alignment procedure initially considered 22 atoms, of which one atom was excluded due to high deviation (RMSD = 3.41 Å during cycle 1). The final alignment was therefore calculated over 21 atoms, yielding an overall RMSD value of 2.998 Å. This result indicates a reasonable structural similarity between the two conformations, while also highlighting subtle deviations that may arise from conformational flexibility or substituent effects.

Table 7
Comparison of thermodynamic properties for Molecule **7** and Molecule **5.**

Property	Molecule 7	Molecule 5
Temperature	298.150 Kelvin	298.150 Kelvin
Pressure	1.00000 atm	1.00000 atm
Thermal Energy Correction	0.262716 Hartree (7.159 eV)	0.324054 Hartree (8.825 eV)
Thermal Enthalpy Correction	0.263660 Hartree (7.185 eV)	0.324998 Hartree (8.850 eV)
Thermal Free Energy Correction	0.192282 Hartree (5.239 eV)	0.250788 Hartree (6.824 eV)
Heat Capacity (Cv)	71.008 cal/mol-K	79.871 cal/mol-K
Entropy (S)	150.228 cal/mol-K	156.188 cal/mol-K
E (Thermal)	164.857 kcal/mol	203.347 kcal/mol

3.3.3. Molecular docking studies

Molecular docking studies provide detailed studies of interactions with specific target receptors, clarifying the focus of research and providing important information about the potential activities of molecules [34].

In this study, three proteins, 3LD6 (human lanosterol 14alpha-demethylase (CYP51) in complex with ketoconazole), 3QLY (*Candida glabrata* dihydrofolate reductase complexed with NADPH and 6-methyl-5-[3-methyl-3-(3,4,5-trimethoxyphenyl)but-1-yn-1-yl]pyrimidine-2,4-diamine (UCP115A)) and 4CCQ (the thioredoxin reductase from *Entamoeba histolytica* with NADP), were used to perform docking analyses with the synthesized molecules (**5** and **7**) and reference drugs (**Fluconazole, Metronidazole, Micanozole**).

3LD6 represents the crystal structure of ketoconazole bound to the human lanosterol 14α-demethylase (CYP51) enzyme. CYP51 is a critical cytochrome P450 enzyme in sterol biosynthesis and plays a role in cholesterol synthesis in human cells. **Ketoconazole** gains antifungal properties by inhibiting the CYP51 enzyme. In fungal cells, CYP51 is involved in ergosterol biosynthesis. Ergosterol is a basic component of the fungal cell membrane, and disruption of its synthesis disrupts the structural integrity of the cell membrane. Inhibition of CYP51 prevents ergosterol synthesis, leading to the accumulation of toxic sterols and death of the fungal cell. Therefore, selective inhibition of CYP51 is an important strategy in antifungal therapy. Azole antifungals (fluconazole, itraconazole, voriconazole, etc.) are effective by targeting this enzyme [32].

3QLY represents the crystal structure of the dihydrofolate reductase (DHFR) enzyme from *Candida glabrata* complexed with NADPH and an inhibitor called UCP115A. Dihydrofolate reductase (DHFR) is an enzyme that plays a vital role in folate metabolism and is required for DNA synthesis and cell division. The DHFR enzyme is found in all living organisms, but there are structural differences between pathogenic fungi and human DHFR. These differences can be targeted for antifungal drug development. UCP115A is a small molecule that inhibits *C. glabrata* DHFR. This inhibitor binds to the enzyme's active site, stops its function, and prevents cellular division by disrupting folate metabolism. This stops the growth of the fungus and provides a potential antifungal effect [34,35].

4CCQ represents the crystal structure of thioredoxin reductase (TrxR) enzyme of *Entamoeba histolytica* in the form of NADP bound. *E. histolytica* is a pathogenic protozoan that causes serious infections such as amoebic dysentery and liver abscess in humans. The main treatment used today is based on drugs such as metronidazole. TrxR plays a critical role in maintaining cellular redox balance and combating oxidative stress. In addition, this enzyme is essential for the survival of the parasite. Molecules that inhibit TrxR can disrupt the redox balance of the parasite and cause cell death. Therefore, TrxR stands out as a potential target for the development of new treatment strategies against amoebic infections [33].

Molecule **5** showed conventional hydrogen bond was observed between THR135, ARG382 and TYR131 amino acids with the 1.93, 1.66 and 1.87 Å bond length, respectively (Fig. 10). Carbon hydrogen bond interaction with GLU443 (3.29 Å), π-sigma interaction with MET380 (3.80 Å), π-π T-Shaped interaction was between TRY131 (3.69 Å). Also π-sulfur interaction with MET380 (4.47 Å), alkyl interaction with CYS449 (4.32 Å). All interactions are shown in detail in ***SI-*** Table 2.

Molecule **7** showed conventional hydrogen bond was observed between HIS447 and LYS156 amino acids with the 2.45 and 1.60 Å bond lengths, respectively (Fig. 11). π-π T-shaped interaction was between PHE152 (4.81 Å), alkyl interaction with MET380 (4.82 Å), and π-Sigma interaction with PHE139 (3.98 Å). Also π-Alkyl interaction with HIS447, TYR131, ILE450 and LYS156 amino acids with the 5.14, 4.92, 5.18 and 4.64 Å bond lengths, respectively. Van der Waals interactions were observed between GLY307, ALA311, TYR145, ARG382, CYS449, ARG448, LEU159 and ALA144. All interactions are shown in detail in ***SI-*** Table 3.

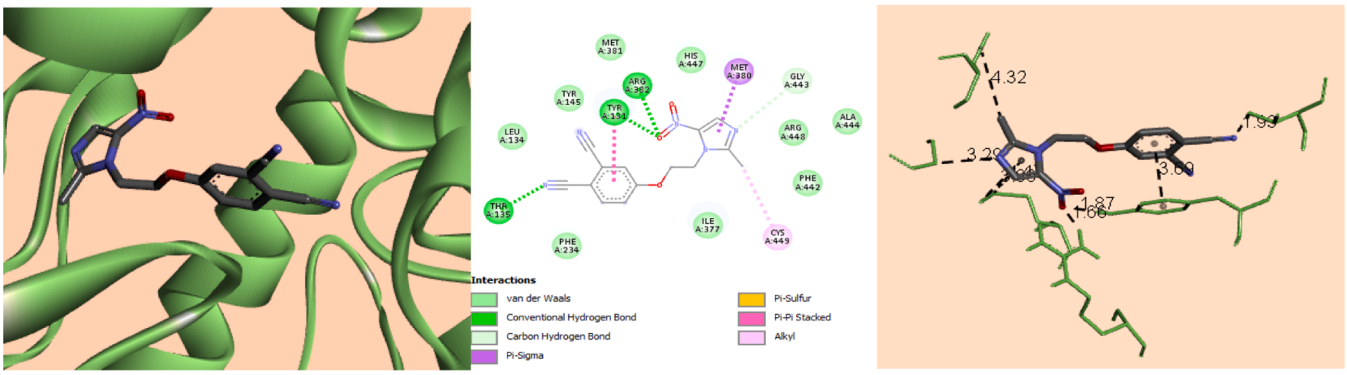

Fig. 10. Docking interactions between the protein **3LD6** and the molecule **5** as the active molecule in database.

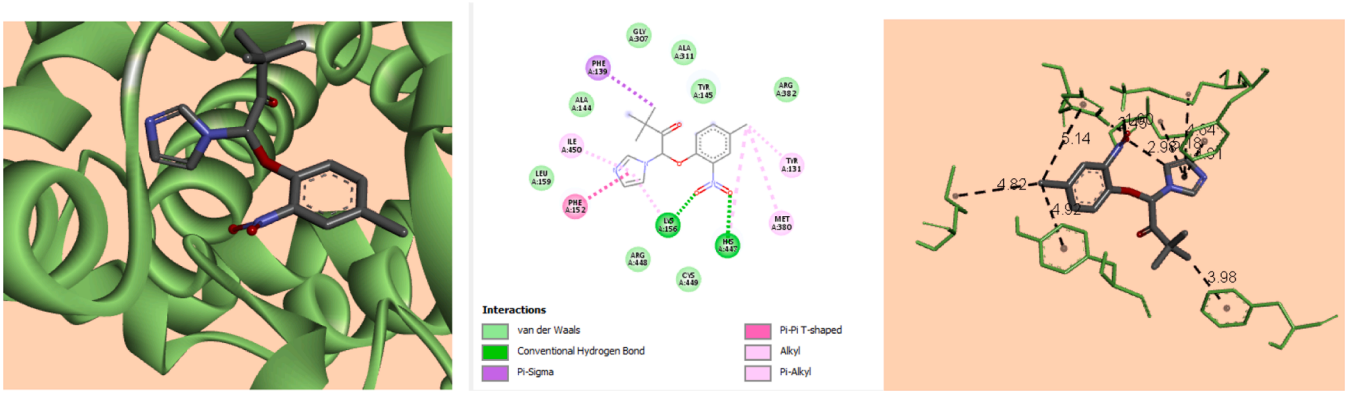

Fig. 11. Docking interactions between the protein 3LD6 and the molecule **7** as the active crystal in database.

Molecule **5** showed conventional hydrogen bonds were observed between ARG188, ARG184, ARG183, GLY161, GLY160 amino acids with the 2.03 and 2.57, 2.32, 1.77, 3.03 and 2.08 Å bond length, respectively (Fig. 12). Carbon Hydrogen bond were observed between ILE246 (3.25 Å), and HIS182 (3.26 Å), π-Sigma interaction with ILE246 (3.58 Å), alkyl interaction with ILE246 (5.14 Å). Also π-Alkyl interaction with ARG188 and ARG183 amino acids with the 5.11 and 4.46 Å bond length, respectively. All interactions are shown in detail in ***SI-*** Table 4

Molecule **7** showed conventional hydrogen bond was observed between LYS122, ARG188, ARG183, ARG188, ARG184 and ARG184 amino acids with the 2.27, 2.25, 2.06, 1.99, 2.01 and 2.79 Å bond length, respectively (Fig. 13). Carbon Hydrogen Bond was observed between HIS182 (3.57 Å), π-cation interaction with ARG183 (4.19 Å), alkyl interaction with ARG183 (4.08 Å). Also π-Alkyl interaction with HIS182 amino acid with the 4.65 Å bond length. All interactions are shown in detail in ***SI-*** Table 5.

Molecule **5** showed conventional hydrogen bond was observed between ALA11 amino acid with the 2.33 Å bond length. Carbon Hydrogen Bond was observed between MET33 (3.20 Å), π-Donor interaction was observed between TYR127 (2.95 Å). π−π T-shaped interaction was found PHE36 with 3.93 Å bond length (Fig. 14). alkyl interactions existed between amino acids ALA11 and LEU25 amino acids with the 4.08 and 4.23 Å bond length, respectively. π-alkyl interactions existed between amino acid ALA11, LEU25, ILE19, and VAL10 amino acids with

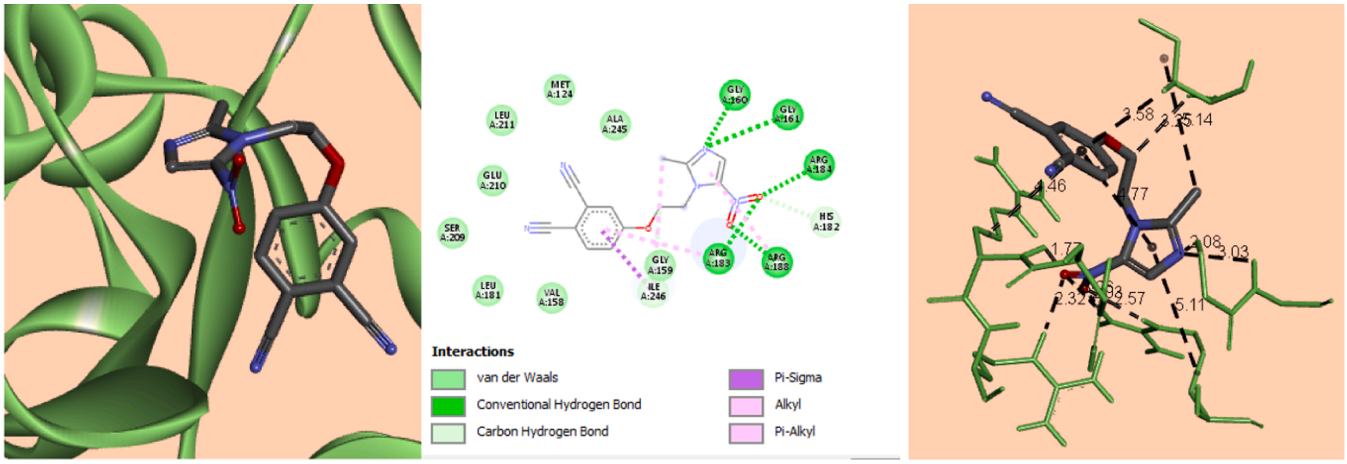

Fig. 12. Docking interactions between the protein 4CCQ and the molecule **5** as the active molecule in database.

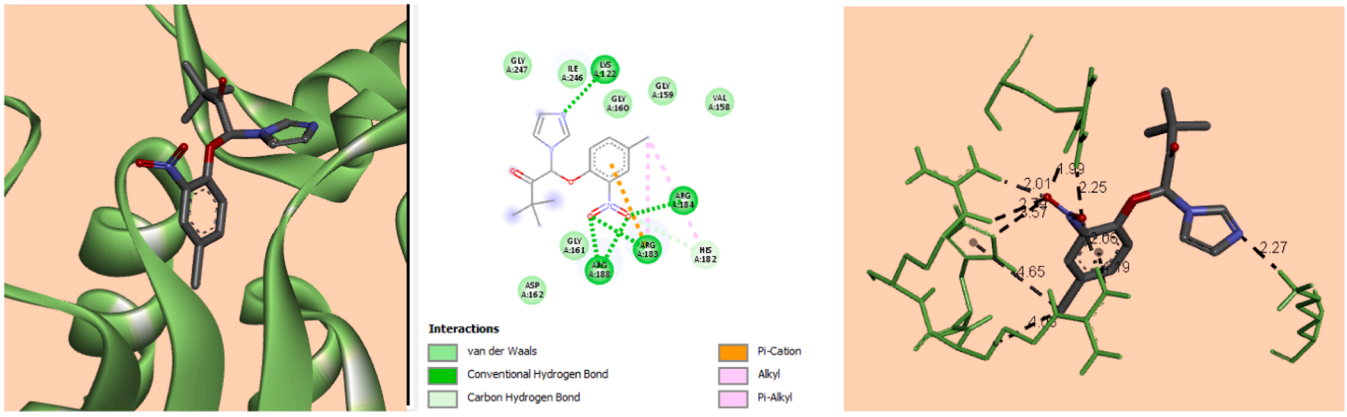

Fig. 13. Docking interactions between the protein 4CCQ and the molecule **7** as the active crystal in database.

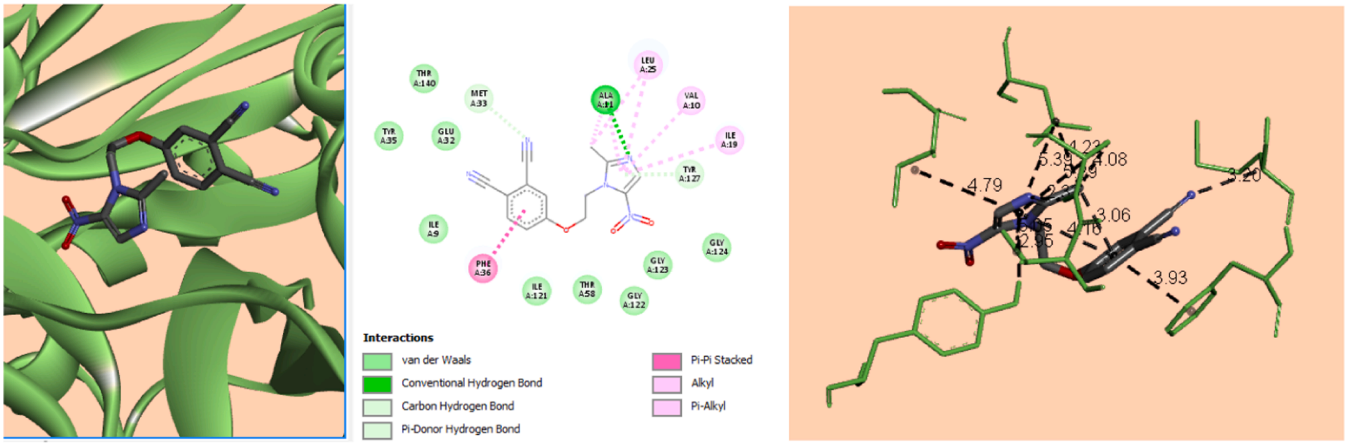

Fig. 14. Docking interactions between the protein **3QLY** and the molecule **5** as the active molecule in database.

the 5.29, 5.39, 4.79 and 5.05 Å bond length, respectively. All interactions are shown in detail in ***SI-*** Table 6.

Molecule **7** exhibited conventional hydrogen bonding interactions with ALA11 (2.14 Å and 2.24 Å), and conventional hydrogen bond was observed with TYR127 (2.00 Å) (Fig. 15). Carbon Hydrogen Bond was observed between VAL10 (3.02 Å), ILE121 (3.53 and 3.34 Å), Amide-pi stacked VAL10 (4.64 Å). Alkyl interactions existed between amino acids ILE19, ILE121, LEU69 and ILE62 amino acids with the 4.39, 4.97, 4.94 and 4.84 Å bond length, respectively. π-alkyl interactions existed between amino acids PHE36, ILE9, ILE19 and LEU25 amino acids with the 4.31, 4.60, 5.35 and 5.33 Å bond length, respectively. All interactions are shown in detail in ***SI-*** Table 7.

Fluconazole exhibited conventional hydrogen bonding interactions with MET381 (2.78 Å), and π-donor Hydrogen bond was observed with HIS236 (2.47 Å) (Fig. 16). π-π T-shaped was observed between HIS236 (4.55 Å), Halogen (Fluorine) interactions with ILE379 (3.02), π-sigma ILE379 (3.83 Å). π-alkyl interactions existed between amino acids ILE379, MET381 and LEU240 amino acids with the 4.90, 5.28 and 5.37 Å bond length, respectively. π-sulfur interactions existed between amino acids MET381, CYS402 and MET100 amino acids with the 4.89, 4.46

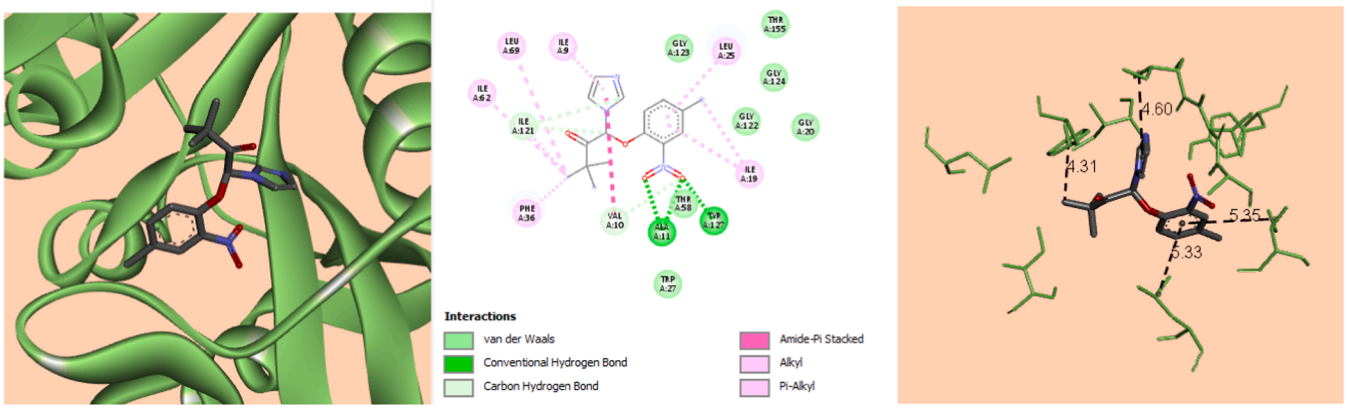

Fig. 15. Docking interactions between the protein **3QLY** and the crystal **7** as the active molecule in database.

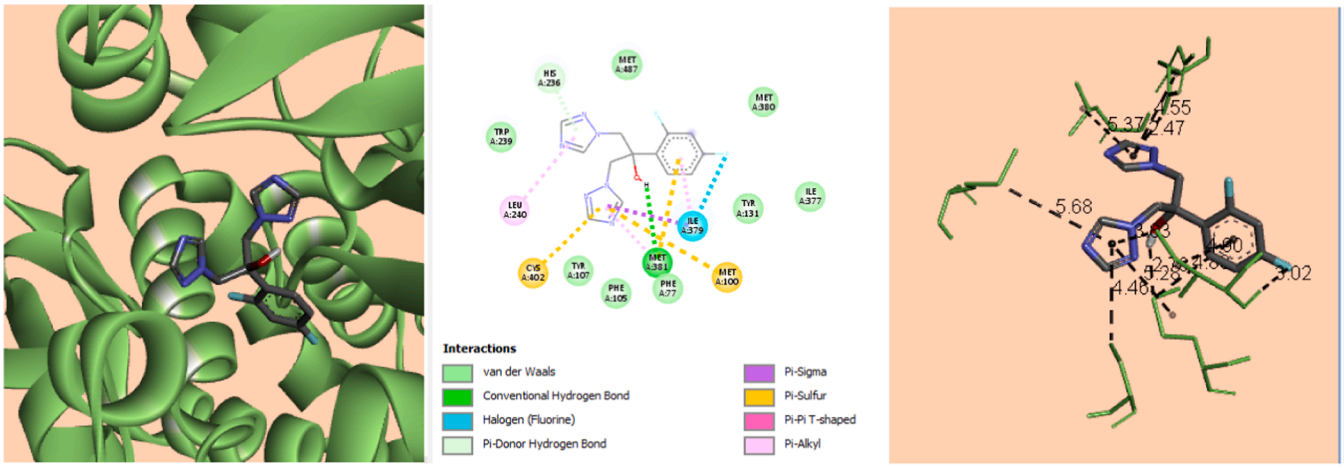

Fig. 16. Docking interactions between the protein **3LD6** and the **Fluconazole** as the active molecule in database.

and 5.68 Å bond length, respectively. All interactions are shown in detail in ***SI-*** Table 8.

Micanozole exhibited carbon hydrogen bonding interactions with ILE19 (3.70 Å), and ILE121 (3.79 Å), and π-Donor Hydrogen bond was observed with GLY123 (2.69 Å) (Fig. 17). π-π T-shaped was observed with TYR127 (5.52 Å). Alkyl interactions existed between LEU25, ALA11, ILE9, ILE62 and LEU69 amino acids with the 4.17, 3.41, 3.98, 4.70 and 4.65 Å bond length, respectively. π-alkyl interactions existed between ILE19, ALA11, TRP27, ILE9, PHE36, PHE36 and MET33 amino acids with the 4.94, 4.15, 5.14, 5.42, 4.71, 4.57 and 5.16 Å bond length, respectively. All interactions are shown in detail in ***SI-*** Table 9.

Metronidazole exhibited conventional hydrogen bonding interactions with Arg183 (1.97 and 1.69 Å), Hıs182 (2.08 Å), Arg184 (2.22 Å and 2.31 Å), Arg188 (2.22 Å and 2.34 Å) (Fig. 18). Carbon Hydrogen bond was observed between HIS182 (3.25 Å), π-cation interaction ARG183 (4.43 Å). Alkyl interactions existed between ILE246 (4.89 Å), π-alkyl interactions existed between ARG188 with the 5.37 Å bond length. All interactions are shown in detail in ***SI-*** Table 10. The results of all docking studies are given in Table 8.

According to the docking results for Thioredoxin Reductase from *Entamoeba histolytica* (EhTrxR) (PDB ID: 4CCQ), the activity order of the molecules was as follows: Molecule **5** (−9.17) > Crystal **7** (−7.79) > **Metronidazole** (−6.13). Molecules **5** and **7** exhibited higher activity than the Metronidazole drug.

For **Lanosterol 14alpha-Demethylase (CYP51) Antibacterial (PDB ID:3LD6)**, the activity order of the molecules was as follows: Molecule **5** (−8.83) > Crystal **7** (−7.20) > **Fluconazole** (−5.65). Molecules **5** and **7** exhibited higher activity than the **Fluconazole** drug.

In the case of ***Candida Glabrata*** **Dihydrofolate Reductase (CoDHFR) Antifungal (PDB ID:3QLY)** the activity order of the molecules was as follows: **Micanozole** (−7.87) > Molecule **5** (−7.64) > Crystal **7** (−7.40). It was observed that molecules **5** and **7** showed similar activity with the drug Micanozole.

Table 8
The results of all docking studies.

Ligand	Thioredoxin Reductase From Entamoeba *Histolytica Antiamoebic* (EhTrxR) (PDB ID:4CCQ)	Lanosterol 14alpha-Demethylase (CYP51) Antibacterial (PDB ID:3LD6)	*Candida Glabrata* Dihydrofolate Reductase (CoDHFR) Antifungal (PDB ID:3QLY)
Molecule 5	**−9.17**	−8.53	−7.64
Crystal 7	−7.79	−7.20	−7.40
Fluconazole	–	- 5.65	–
Metronidazole	- 6.13	–	–
Micanozole	–	–	**7.87**

4. Conclusion and discussion

This study comprehensively investigated new metronidazole derivative Molecule **5** and climbazole derivative Molecule **7** at structural and electronic levels. The geometries were optimized using DFT, and their electronic energy, dipole moment, HOMO–LUMO gaps, molecular electrostatic potential maps, and thermodynamic parameters were compared. Molecule **5** showed lower total energy, indicating higher structural stability, whereas Molecule **7** exhibited higher polarity, suggesting stronger interactions in biological environments. HOMO–LUMO gap analysis revealed reactivity differences, and MEP maps visualized electrophilic and nucleophilic regions.

Hirshfeld surface analysis revealed that H•••Cl/Cl•••H and N•••H/H•••N contacts play a major role in crystal packing. Energy framework analysis showed that dispersion energies are the dominant contributors to structural stability.

Molecular docking studies demonstrated that both molecules possess strong antifungal activity, comparable to fluconazole, and remain stable in their active conformations when interacting with the 14α-demethylase enzyme. Antiamoebic potential was also confirmed, with strong and specific ligand–residue interactions observed for the EhTrR protein.

Overall, these findings support the rational design of next-generation molecules with dual antiamoebic and antifungal activities and validate DFT calculations and molecular docking as powerful predictive tools. Future studies should experimentally confirm these results and explore the development of novel analogs.

Data availability

The data that support the findings of this study are available from the corresponding author upon reasonable request.

CRediT authorship contribution statement

Ebrar Nur Özkan: Writing – review & editing, Methodology, Investigation, Formal analysis, Conceptualization. **Melek Gökmen Karakaya:** Conceptualization, Data curation, Investigation, Methodology, Project administration, Supervision, Writing – review & editing. **Özlem Gündoğdu Aytaç:** Writing – review & editing, Investigation, Formal analysis. **Ertan Şahin:** Writing – review & editing, Investigation, Formal analysis. **Abdullah Menzek:** Data curation, Investigation, Methodology, Writing – review & editing.

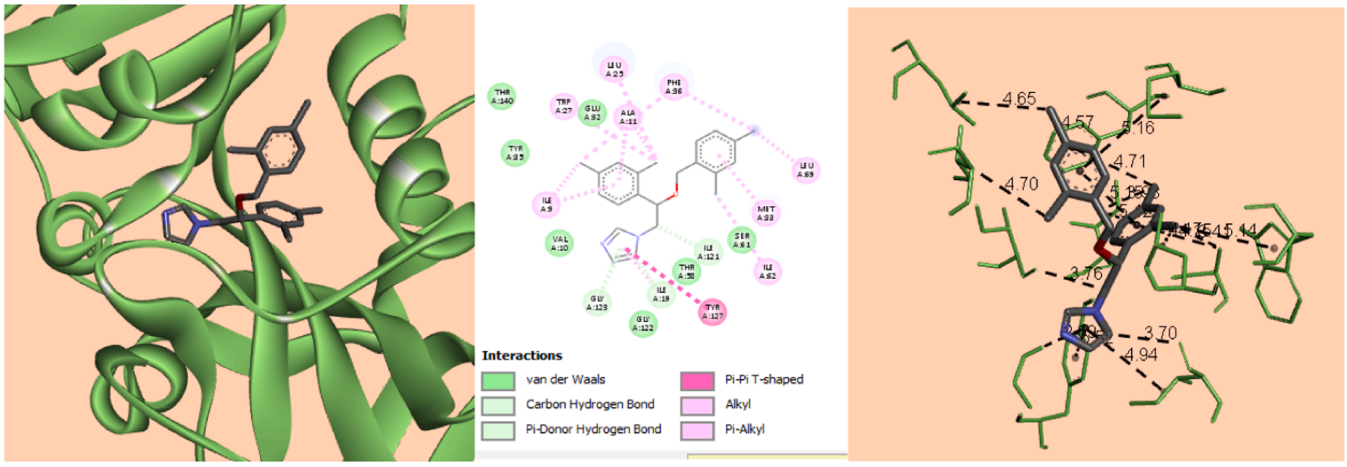

Fig. 17. Docking interactions between the protein **3QLY** and the **Micanozole** as the active molecule in database.

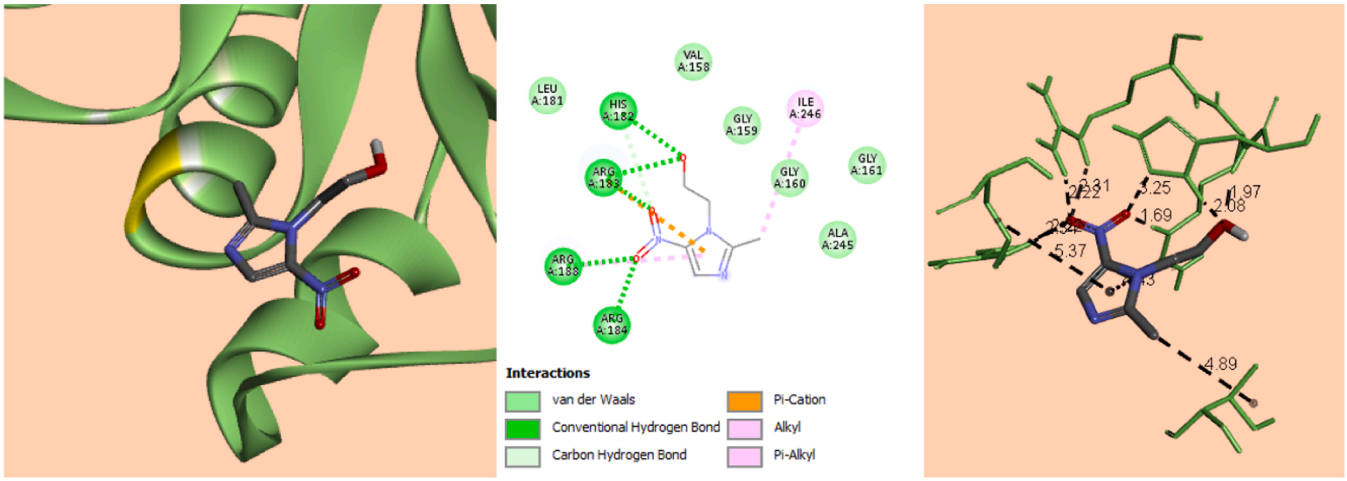

Fig. 18. Docking interactions between the protein **4CCQ** and the **Metronidazole** as the active molecule in database.

Declaration of competing interest

The authors declare that they have no known competing financial interests or personal relationships that could have appeared to influence the work reported in this paper.

Acknowledgements

This study was financially supported by Uşak University Scientific Research Projects Coordination Unit (Project no. 2015/MF008 and Project name Synthesis of Climbazole and Metronidazole Derivatives). The authors thank to Atatürk University, Science Faculty, Department of Chemistry and Uşak University Scientific Research Projects Coordination Unit and Uşak University Banaz Vocational School.

Supplementary materials

Supplementary material associated with this article can be found, in the online version, at doi:10.1016/j.molstruc.2025.144223.

References

[1] X.C. Yang, C.M. Zeng, S.R. Avula, X.M. Peng, R.X. Geng, C.H. Zhou, Novel coumarin aminophosphonates as potential multitargeting antibacterial agents against Staphylococcus aureus, Eur. J. Med. Chem. 245 (2023) 114891, https://doi.org/10.1016/j.ejmech.2022.114891.

[2] H.R. Rashdan, A.H. Abdelmonsef, M.M. Abou-Krisha, T.A. Yousef, Synthesis, identification, computer-aided docking studies, and ADMET prediction of novel benzimidazo-1,2,3-triazole based molecules as potential antimicrobial agents, Molecules 26 (23) (2021) 7119, https://doi.org/10.3390/molecules26237119.

[3] X. Zhou, K. Zhang, S. Ding, L. Wang, M. Li, K. Wang, G. Wu, Cascade reaction of isocyanides with carboxylic acid and cd_3sso_3na: toward S-CD_3 thiocarbamates, Org. Lett. 27 (18) (2025) 4742–4746, https://doi.org/10.1021/acs.orglett.5c01166.

[4] Y. Lou, F. Song, M. Cheng, Y. Hu, Y. Chai, Q. Hu, Y. Zhang, Effects of the CYP3A inhibitors, voriconazole, itraconazole, and fluconazole on the pharmacokinetics of osimertinib in rats, PeerJ 11 (2023) e15844, https://doi.org/10.7717/peerj.15844.

[5] P. Bellala, M. Gundluru, K.K. Konidala, S. Yeguvapalli, P. Itte, S. Poreddy, S. Sarva, S.R. Cirandur, CF3 functionalized pyridinyl α-aminophosphonates as potential antimicrobials: green synthesis, bio-assay, DFT calculations, molecular docking and ADMET studies, J. Mol. Struct. (2025) 143549, https://doi.org/10.1016/j.molstruc.2025.143549.

[6] S.M. Boddapati, R. Tamminana, H.J. Senapathi, A.E. Kola, S.A. Ansari, R. K. Kapavarapu, H.B. Bollikolla, S.B. Jonnalagadda, An efficient Cu catalyzed regioselective ortho-nitration approach for the synthesis of 2-nitroarylcyanamides: molecular docking and ADME studies, J. Mol. Struct. 1329 (2025) 141409, https://doi.org/10.1016/j.molstruc.2025.141409.

[7] Q. Guan, S. Xing, L. Wang, J. Zhu, C. Guo, C. Xu, Q. ZhÅ, Y. Wu, Y. Chen, H. Sun, Triazoles in medicinal chemistry: physicochemical properties, bioisosterism, and application, J. Med. Chem. 67 (10) (2024) 7788–7824, https://doi.org/10.1021/acs.jmedchem.4c00652.

[8] J. Devasia, A. Nizam, V.L. Vasantha, Azole-based antibacterial agents: a review on multistep synthesis strategies and biology, Polycycl. Aromat. Compd. 42 (8) (2022) 5474–5495, https://doi.org/10.1080/10406638.2021.1938615.

[9] J.J. McKinnon, D. Jayatilaka, M.A. Spackman, Towards quantitative analysis of intermolecular interactions with Hirshfeld surfaces, Chem. Commun. (2004) 3814–3816, https://doi.org/10.1039/B704980C.

[10] B. Van Vlem, R. Vanholder, P. De Paepe, S. Ringoir, D. Vogelaers, Immunomodulating effects of antibiotics: literature review, Infection 24 (4) (1996) 275–291.

[11] K.C. Lamp, C.D. Freeman, N.E. Klutman, M.K. Lacy, Pharmacokinetics and pharmacodynamics of the nitroimidazole antimicrobials, Clin. Pharmacokinet. 36 (5) (1999) 353–373.

[12] J.S. Simms-Cendan, Metronidazole, Prim. Care Update OB/GYNS 3 (5) (1996) 153–156.

[13] V. Kushwaha, P. Agrawal, V. Shukla, B. Pathak, Metronidazole: drug of choice for anaerobic infections—an overview, World J. Pharm. Res. 11 (2022) 130–141, https://doi.org/10.20959/wjpr202213-25467.

[14] J. Overgaard, Clinical evaluation of nitroimidazoles as modifiers of hypoxia in solid tumors, Oncol. Res. 6 (10–11) (1994) 509–518.

[15] J.G. Rajendran, D.A. Mankoff, F. O'Sullivan, L.M. Peterson, D.L. Schwartz, E. U. Conrad, A.M. Spence, M. Muzi, D.G. Farwell, K.A. Krohn, Hypoxia and glucose metabolism in malignant tumors: evaluation by [18F]fluoromisonidazole and [18F]fluorodeoxyglucose positron emission tomography imaging, Clin. Cancer Res. 10 (7) (2004) 2245–2252, https://doi.org/10.1158/1078-0432.CCR-0688-3.

[16] N. Rani, A. Sharma, G.Kumar Gupta, R. Singh, Imidazoles as potential antifungal agents: a review, Mini Rev. Med. Chem. 13 (11) (2013) 1626–1655.

[17] W. Song, N. Wang, A. Li, X. Ji, X. Huang, T. Wang, H. HÅ, Multi-component crystal strategy for improving water solubility and antifungal activity of Climbazole, Pharm. Res. 41 (8) (2024) 1737–1754, https://doi.org/10.1007/s11095-024-03748-5.

[18] M.G. Karakaya, B. Gezer, A. Menzek, Ö.G. Aytaç, Removal of heavy metal iron(II) ions from wastewater using an ultrasonic system with climbazole-alcohol, Turk. J. Chem. 49 (2025) 279–292, https://doi.org/10.55730/1300-0527.3729.

[19] S. Patterson, S. Wyllie, Nitro drugs for the treatment of trypanosomatid diseases: past, present, and future prospects, Trends Parasitol. 30 (6) (2014) 289–298, https://doi.org/10.1016/j.pt.2014.04.003.

[20] A.M.M. Hassan, A.F. Mohammed, J. Kumari, D. Sriram, H.H. Abdu-Allah, S.G. A. Abdel-Moty, Hybrids of 4-aminosalicylic acid with dual anti-mycobacterial and anti-inflammatory activities: synthesis, biological evaluation, in silico investigation and structure-activity relationships exploration, J. Mol. Struct. (2024) 139217, https://doi.org/10.1016/j.molstruc.2024.139217.

[21] S. Suda, A. Tateno, D. Nakane, T. Akitsu, Hirshfeld surface analysis for investigation of intermolecular interaction of molecular crystals, Int. J. Org. Chem. 13 (2) (2023) 57–85.

[22] A.B. Ibragimov, J.M. Ashurov, B.T. Ibragimov, A.G. Eshimbetov, S.S. Azimova, Z. G. Tilyakov, A.F. Dusmatov, Synthesis, structure, Hirshfeld surface analysis of the new copper complex of 3,5-dinitrobenzoic acid and docking study of its metal complexes bioactivity, J. Mol. Struct. 1292 (2023) 136105, https://doi.org/10.1016/j.molstruc.2023.136105.

[23] S.K. Seth, Structural elucidation and contribution of intermolecular interactions in O-hydroxy acyl aromatics: insights from X-ray and Hirshfeld surface analysis, J. Mol. Struct. 1064 (2014) 70–75, https://doi.org/10.1016/j.molstruc.2014.01.068.

[24] A.M. Senol, C. Bayrak, A. Menzek, Y. Onganer, N. Yaka, Synthesis and photophysical properties of new pyrazolines with triphenyl and ester derivatives, J. Mol. Struct. 1214 (2020) 128213, https://doi.org/10.1016/j.molstruc.2020.128213.

[25] C. Bayrak, P. Taslimi, N. Kilinc, I. Gulcin, A. Menzek, Synthesis and biological activity of some bromophenols and their derivatives including natural products, Chem. Biodivers. 20 (2023) e202300469, https://doi.org/10.1002/cbdv.202300469.

[26] Rigaku/MSC, Inc., 9009 new Trails Drive, the Woodlands, TX 77381.

[27] G.M. Sheldrick, SHELXS-97 and SHELXL-97, Program for Crystal Structure Solution and Refinement, University Göttingen, Göttingen, Germany, 1997.

[28] M.A. Spackman, P.G. Byrom, A novel definition of a molecule in a crystal, Chem. Phys. Lett. 267 (3–4) (1997) 215–220.

[29] H. Tandon, T. Chakraborty, V. Suhag, A brief review on importance of DFT in drug design, Res. Med. Eng. Sci. 7 (4) (2019), https://doi.org/10.31031/RMES.2019.07.00068.

[30] M.J. Frisch, G.W. Trucks, H.B. Schlegel, G.E. Scuseria, M.A. Robb, J.R. Cheeseman, G. Scalmani, V. Barone, G.A. Petersson, H. Nakatsuji, X. Li, M. Caricato, A. Marenich, J. Bloino, B.G. Janesko, R. Gomperts, B. Mennucci, H.P. Hratchian, J.V. Ortiz, A.F. Izmaylov, J.L. Sonnenberg, D. Williams-Young, F. Ding, F. Lipparini, F. Egidi, J. Goings, B. Peng, A. Petrone, T. Henderson, D. Ranasinghe, V.G. Zakrzewski, J. Gao, N. Rega, G. Zheng, W. Liang, M. Hada, M. Ehara, K. Toyota, R. Fukuda, J. Hasegawa, M. Ishida, T. Nakajima, Y. Honda, O. Kitao, H. Nakai, T. Vreven, K. Throssell, J.A. Montgomery, Jr., J.E. Peralta, F. Ogliaro, M. Bearpark, J. J. Heyd, E. Brothers, K.N. Kudin, V.N. Staroverov, T. Keith, R. Kobayashi, J. Normand, K. Raghavachari, A. Rendell, J.C. Burant, S.S. Iyengar, J. Tomasi, M. Cossi, J.M. Millam, M. Klene, C. Adamo, R. Cammi, J.W. Ochterski, R.L. Martin, K. Morokuma, O. Farkas, J.B. Foresman, and D.J. Fox, Gaussian 09, Revision A.02, Gaussian, Inc., Wallingford CT, 2016.

[31] K. Ozturk, E.N. Ozkan, C.E. Caliskan, S. Aytac, O.G. Aytac, Synthesis, single crystal XRD, DFT, molecular docking studies and antioxidant capacity and antibacterial evaluation of β-phenylethylamine derivative schiff base compound, J. Mol. Struct. (2025) 143011, https://doi.org/10.1016/j.molstruc.2025.143011.

[32] J. Soni, N. Sahiba, A. Sethiya, P. Teli, D.K. Agarwal, A. Manhas, P.C. Jha, D. Joshi, S. Agarwal, Biscoumarin derivatives as potent anti-microbials: graphene oxide catalyzed eco-benign synthesis, biological evaluation and docking studies, Polycycl. Aromat. Compd. 42 (6) (2022) 2970–2990, https://doi.org/10.1080/10406638.2020.1852277.

[33] A. Khaldan, K. El khatabi, R. El-mernissi, A. Sbai, M. Bouachrine, T. Lakhlifi Combined 3D-QSAR modeling and molecular docking study on metronidazole-triazole-styryl hybrids as antiamoebic activity, Moroccan J. Chem. 8 (2020), https://doi.org/10.48317/IMIST.PRSM/morjchem-v8i2.19099. J-Chem.

[34] F.S. Tokali, P. Taslimi, I.H. Demircioglu, K. Sendil, B. Tuzun, I. Gulcin, Novel phenolic Mannich base derivatives: synthesis, bioactivity, molecular docking, and ADME-tox studies, J. Iran. Chem. Soc. 19 (2022) 563–577, https://doi.org/10.1007/s13738-021-02331-8.

[35] M. Singh, M. Raghav, A. Singh, A. Kumari, P. Bansal, S. Prakash, A. Kumar, Interaction of pteridophytic bioactive compounds with fungal dihydrofolate reductase enzyme as inhibitor, J. Fac. Pharm. 47 (2023) 1170–1176, https://doi.org/10.33483/jfpau.1270767.

[36] F. Lv, B. CÅ, Y. Cui, T. Liu, Zinc phthalocyanine labelled polyethylene glycol: preparation, characterization, interaction with bovine serum albumin and near infrared fluorescence imaging in vivo, Molecules 17 (2012) 6348–6361, https://doi.org/10.3390/molecules17066348.

[37] T.M. Keller, Synthesis and polymerization of multiple aromatic ether phthalonitriles, Chem. Mater. 6 (1994) 302–305.

[38] J.G. Young, W, Onyebuagu Synthesis and characterization of Di-disubstituted phthalocyanines, J. Org. Chem. 55 (1990) 2155–2159.

[39] Z. Kelesoglu, E.C. Kaya, A.A. Kaya, H. Kantekin, O. Buyukgungor, 4-[2-(Cyclohexa-1,4-dien-1-yl)ethoxy]benzene-1,2-dicarbonitrile, Acta Crystallogr. Sect. E Struct. Rep. Online 67 (11) (2011) o2989, https://doi.org/10.1107/S1600536811042164.

[40] Y. Cetinkaya, A. Menzek, E. Sahin, H.T. Balaydin, Selective O-demethylation during bromination of (3,4-dimethoxyphenyl)(2,3,4-trimethoxyphenyl) methanone, Tetrahedron 67 (19) (2011) 3483–3487, https://doi.org/10.1016/j.tet.2011.03.033.

[41] K.V. Drozd, A.N. Manin, D.E. Boycov, A.V. Churakov, G.L. Perlovich, Pharmaceutical multi-component crystals of antifungal drugs with improved dissolution performance, Cryst. Growth Des. 21 (12) (2021) 7285–7297, https://doi.org/10.1021/acs.cgd.1c01139.?urlappend=%3Fref%3DPDF&jav=VoR&rel=cite-as.

[42] P.R. Spackman, M.J. Turner, J.J. McKinnon, S.K. Wolff, D.J. Grimwood, D. Jayatilaka, M.A. Spackman, CrystalExplorer: a program for Hirshfeld surface analysis, visualization and quantitative analysis of molecular crystals, J. Appl. Crystallogr. 54 (2021) 1006–1011, https://doi.org/10.1107/S1600576721002910.

[43] G.R. Desiraju, Kristal mühendisliğinde hidrojen köprüleri: sınırları olmayan etkileşimler, Acc. Chem. Res. 35 (2002) 565–573, https://doi.org/10.1021/ar010054t.

[44] R.S. Rowland, R. Taylor, Intermolecular nonbonded contact distances in organic crystal structures: comparison with distances expected from van der Waals radii, J. Phys. Chem. 100 (1996) 7384–7391, https://doi.org/10.1021/jp953141+.

[45] E. Meier, W. Seichter, M. Mazik, Combination of hydrogen and halogen bonds in the crystal structures of 5-halogeno-1H-isatin-3-oximes: involvement of the oxime functionality in halogen bonding, Molecules 29 (2024) 1174, https://doi.org/10.3390/molecules29051174.

[46] Campbell F. Mackenzie, a Peter R. Spackman, a Dylan Jayatilakaa and Mark A. Spackman, CrystalExplorer model energies and energy frameworks: extension to metal coordination compounds, organic salts, solvates and open-shell systems crossmark logo IUCrJ, 4, 2017, 575–587 ISSN: 2052-2525. https://doi.org/10.1107/S205225251700848X.

[47] A.U. Kumar, K.J. Pampa, K. Kumara, M.K. Hema, N.V. Harohally, N.K. Lokanath, Structural-property relationship in halogen-bonded Schiff base derivative: crystal structure, computational and SARS-CoV-2 docking studies, J. Mol. Struct. 1265 (2022) 133409, https://doi.org/10.1016/j.molstruc.2022.133409.

[48] C. Kalaiarasi, C. George, R.G. Gonnade, V.R. Hathwar, K. Poomani, Experimental and theoretical charge density, intermolecular interactions and electrostatic properties of metronidazole, Acta Crystallogr. B Struct. Sci. Cryst. Eng. Mater. 75 (2019) 942–953, https://doi.org/10.1107/S2052520619011272.

[49] N.M. Blaton, O.M. Peeters, C.J. De Ranter, 2-(2-Methyl-5-nitro-1-imidazolyl) ethanol (metronidazole), Acta Crystallogr. B Struct. Sci. 35 (1979) 2465–2467, https://doi.org/10.1107/S0567740879009663.

[50] G.R. Desiraju, G.W. Parshall, Crystal engineering: the design of organic solids, Mater. Sci. Monogr. (1989) 54. http://pascal-francis.inist.fr/vibad/index.php?action=getRecordDetail&idt=6688483.

[51] F. Jensen, Introduction to Computational Chemistry, John Wiley & Sons, 2017.

[52] R.G. Parr, Density functional theory of atoms and molecules, in: Horizons of Quantum Chemistry: Proceedings of the Third International Congress of Quantum Chemistry, Kyoto, Japan, Springer, 1989, pp. 5–15, https://doi.org/10.1007/978-94-009-9027-2_2. October 29–November 3, 1979Dordrecht.

[53] W. Koch, M.C. Holthausen, A Chemist's Guide to Density Functional Theory, John Wiley & Sons, 2015.

[54] P. Atkins, J. De Paula, Physical Chemistry, 1, Macmillan, 2006.

[55] F. Aiga, T. Tada, R. Yoshimura, Frequency-dependent polarizabilities, hyperpolarizabilities, and excitation energies from time-dependent density-functional theory based on the quasienergy derivative method, J. Chem. Phys. 111 (7) (1999) 2878–2888, https://doi.org/10.1063/1.479570.

[56] N.T. Anh, Frontier Orbitals: a Practical Manual, John Wiley & Sons, 2007.

[57] J.S. Murray, Atoms in molecules without boundaries: analyses via electrostatic potentials at nuclei, Struct. Chem. 35 (5) (2024) 1355–1364, https://doi.org/10.1007/s11224-024-02369-3.

[58] D.H. Pereira, F.A. La Porta, R.T. Santiago, D.R. Garcia, T.C. Ramalho, New perspectives on the role of frontier molecular orbitals in the study of chemical reactivity: a review, Rev. Virt. Quim. 8 (2) (2016) 425–453, https://doi.org/10.5935/1984-6835.20160032.

[59] S. Sharmila, C. Mahalakshmi, Homo Lumo study, reactivity descriptors and Mulliken charges of imidazole derivative, IRJEdT 5 (4) (2023) 35–38.

[60] J. Yu, N.Q. Su, W. Yang, Describing chemical reactivity with frontier molecular orbitalets, JACS Au 2 (6) (2022) 1383–1394, https://doi.org/10.1021/jacsau.2c00085.
[61] A.H. Bakheit, M.W. Attwa, A.A. Kadi, H.A. Ghabbour, H.M. Alkahtani, Exploring the chemical reactivity, molecular docking, molecular dynamic simulation and ADMET properties of a tetrahydrothienopyridine derivative using computational methods, Crystals 13 (7) (2023) 1020, https://doi.org/10.3390/cryst13071020.
[62] A. Kulandaisamy, M. Panneerselvam, R.V. Solomon, M. Jaccob, J. Ramakrishnan, K. Poomani, M. Maruthamuthu, N. Tharmalingam, Halogen-based 17β-HSD1 inhibitors: insights from DFT, docking, and molecular dynamics simulation studies, Molecules 27 (12) (2022) 3962, https://doi.org/10.3390/molecules27123962.
[63] E.K. Aslan, A. Karagüzel, K. Lam, C. Dengiz, S. Huang, R.J. Burk, R. Salehi, S. J. Sajeevan, G.W. Zamponi, G. Wolber, D.W. Armstrong, M.G. Gündüz, Synthesis, molecular modeling, DFT studies, and enantioseparation of tetrahydro-4H-chromene derivatives with calcium channel blocking activity, J. Mol. Struct. 1330 (2025) 141457, https://doi.org/10.1016/j.molstruc.2025.141457.
[64] Y. Megrouss, Y. Salem, A. Mansour, B. Zohra Douaa, K. Sid Ahmed, H. Benaissi, C. Abdelkader, Molecular structure, lattice energy, Hirshfeld surface and NCI-RDG analysis, DFT calculations, and in silico molecular docking of an imidazole derivative, Phys. Chem. Res. 12 (4) (2024) 975–990, https://doi.org/10.22036/pcr.2024.448149.2495.
[65] S. Süzer, Deposition and stability of metal ions on oxidised silicon surfaces: electrochemical correlation, J. Electron. Spectros. Relat. Phenomena 114 (2001) 1151–1154, https://doi.org/10.1016/S0368-2048(00)00302-9.
[66] P. Politzer, J.S. Murray, T. Clark, Halogen bonding and other σ-hole interactions: a perspective, Phys. Chem. Chem. Phys. 15 (27) (2013) 11178–11189, https://doi.org/10.1039/C3CP00054K.
[67] L. Brammer, A. Peuronen, T.M. Roseveare, Halogen bonds, chalcogen bonds, pnictogen bonds, tetrel bonds and other σ-hole interactions: a snapshot of current progress, Cryst. Struct. Commun. 79 (6) (2023) 204–216, https://doi.org/10.1107/S2053229623004072.
[68] M.L. Bogado, R.N. Villafañe, J.L. Gómez Chavez, E.L. Angelina, G.L. Sosa, N. M. Peruchena, Targeting protein pockets with halogen bonds: the role of the halogen environment, J. Chem. Inf. Model. 62 (2022) 6494–6507, https://doi.org/10.1021/acs.jcim.2c00475.
[69] M.H. Kolar, P. Hobza, Computer modeling of halogen bonds and other σ-hole interactions, Chem. Rev. 116 (2016) 5155–5187, https://doi.org/10.1021/acs.chemrev.5b00560.
[70] P. Politzer, J.S. Murray, Electrostatic potentials at the nuclei of atoms and molecules, Theor. Chem. Acc. 140 (2021) 7, https://doi.org/10.1007/s00214-020-02701-0.